

# **Near-Ultrahigh Pressure Processing of Continental Crust: Miocene Crustal Xenoliths from the Pamir**

Bradley Hacker (corresponding author)

Department of Geological Sciences, University of California, Santa Barbara, CA 93106-9630, USA; hacker@geol.ucsb.edu; ph 805 893 7952; fax 805 893 2314

Peter Luffi

Department of Geology and Geophysics, University of Bucharest, Bucharest, 70139, Romania

Valery Lutkov and Vladislav Minaev

Geological Institute of the Tajik Academy of Science, 734063, Dushanbe, Tajikistan

Lothar Ratschbacher

Institut für Geowissenschaften, Technische Universität Bergakademie Freiberg, 09599 Freiberg, Germany

Terry Plank

Department of Earth Sciences, 685 Commonwealth Avenue, Boston University, Boston MA 02215, USA;

Mihai Ducea

Department of Geosciences, University of Arizona, Tucson, AZ, 85721, USA;

Alberto Patiño-Douce

Department of Geology, University of Georgia, Athens, GA 30602, USA;

Michael McWilliams and Jim Metcalf

Geological and Environmental Sciences, Stanford University, Stanford, CA 94305-2115, USA.

Running title: Xenoliths from ultrahigh-pressure continental crust

Keywords: xenolith; high-pressure; subduction; Pamir; Tibet

*Journal of Petrology* revised version of 12/2004

## **ABSTRACT**

Xenoliths of deep origin hosted by Miocene ultrapotassic rocks in the Southern Pamir bear important new information regarding the geological processes accompanying tectonism during the Indo–Eurasian collision. Four types have been studied: sanidine eclogites (omphacite, garnet, sanidine, quartz, biotite, kyanite), felsic granulites (garnet, quartz, sanidine and kyanite), basaltic eclogites (omphacite and garnet), and a glimmerite (biotite, clinopyroxene and sanidine). Apatite, rutile and carbonate are the most abundant minor phases. Hydrous phases (biotite and phengite in felsic granulites and basaltic eclogites, amphiboles in mafic and sanidine eclogites) and plagioclase form minor inclusions in garnet or kyanite. Solid-phase thermobarometry reveals recrystallization at mainly ultrahigh temperatures of 1000–1100°C and near-ultrahigh pressures of 2.5–2.8 GPa. Textures, parageneses and mineral compositions suggest derivation of the xenoliths from subducted basaltic, tonalitic and pelitic crust that experienced high-pressure dehydration melting, K-rich metasomatism, and solid-state re-equilibration. The timing of these processes is constrained by zircon ages from the xenoliths and  $^{40}\text{Ar}/^{39}\text{Ar}$  ages of the host volcanic rocks to 57–11 Ma. These xenoliths reveal that deeply subducted crust may undergo extensive dehydration-driven partial melting, density-driven differentiation and disaggregation, and sequestration within the mantle. These processes may also contribute to the alkaline volcanism observed in continent-collision zones.

## INTRODUCTION

Exposures of ultrahigh-pressure rocks tell us much about the subduction or foundering and exhumation of continental margins or fragments. These ultrahigh-pressure terranes always undergo significant recrystallization and overprinting during their exhumation, however, such that details about the chemical and physical processing of subducted crustal material at high pressures and high temperatures are invariably erased. Only xenoliths erupted from ultrahigh-pressure settings can provide this important information, but such rocks are exceptionally rare. We report here on the petrology, physical properties, and geochronology of a Miocene xenolith suite from the Pamir that has captured near-ultrahigh-pressure metamorphism in the act. The xenoliths yield insight into the geodynamic effects of the melting, metasomatism, and melt injection that takes place during profound subduction or foundering of continental crust. They also provide information on the deep crust beneath the southern Pamir and Tibet and, together with geologic data from Tibetan xenoliths (Hacker *et al.* 2000), suggest a similar first-order crustal structure for the Pamir and Tibet.

## DUNKELDIK ULTRAPOTASSIC SUITE

The Dunkeldik magmatic field is part of a poorly defined Cenozoic metamorphic and magmatic belt that stretches from the Chinese Pamir through the southern and central Pamir of Tajikistan (Figure 1a) (Vlasov *et al.* 1991; Hubbard *et al.* 1999; Schwab *et al.* 2004). It contains basalts, diorites, granodiorites, and leucogranites with Eocene to late Miocene crystallization ages (Ratschbacher *et al.*, in preparation). The Dunkeldik field

(Figure 1b, 1c) lies between the Late Triassic–Early Jurassic, south-facing Jinsha–Tanymas suture and the Late Jurassic–Early Cretaceous, north-facing Rushan–Pshart–Bangong–Nuijiang suture (Schwab *et al.* 2004) in an area transected by partly active faults related to the Karakoram fault zone (Strecker *et al.* 1995). In the Dunkeldik valley, a series of ~11 Ma old (see below), alkaline volcanic–hypabyssal complexes erupted deep crustal and mantle xenoliths (Dmitriev 1976). The xenolith-bearing igneous suite includes ultrapotassic ( $K_2O/Na_2O = 4.7$ ;  $K_2O = 7.4$  wt%;  $n=9$ ) dikes and subvolcanic bodies that range in composition from alkali basalt (fergusite) to trachyte, syenite, and carbonatite (Dmitriev 1976); xenoliths are found only in the alkali basalts. Abundances of the various xenolith types ( $n > 300$ ) are as follows: 38% eclogite and biotite eclogite, 19% phlogopite pyroxenite and glimmerite (in the sense of Gregoire *et al.* 2002), 15% biotite–garnet clinopyroxenite, 8% biotite–garnet granulite, 6% kyanite–garnet granulite, 4% mafic garnet granulite, 3% phlogopite–garnet websterite, and 7% other rocks (Lutkov 2003).

## ANALYTICAL TECHNIQUES

Textural analysis was accomplished through optical microscopy and back-scattered electron microscopy. Mineral modes were determined by point counting with an optical microscope (Table 1). Mineral compositions were determined using a University of California, Santa Barbara 5-spectrometer Cameca SX-50 operated at 15 kV and 15 nA, and a University of Arizona 4-spectrometer Cameca SX-50 electron microprobe operated at 15 kV and 20 nA, both calibrated with natural and synthetic mineral standards (Table 2). Table 3 gives bulk compositions calculated from mineral modes and mineral compositions. Major- and trace-element compositions were measured at Boston

University using the remains of thin section billets. This is not ideal because the samples are contaminated with epoxy from thin section impregnation, and some include bits of host lava. Billets were first abraded with silicon carbide to remove as much as possible of the epoxy and weathered surfaces, and then powdered in alumina. Major elements were measured by ICP-ES, following  $\text{LiBO}_2$  fusions, and by ICP-MS, following HF-nitric digestions (Table 3, methods described in Kelley *et al.* 2003). Elements measured by both techniques (e.g., Ba) indicate excellent agreement, within 2% relative. Differences among other elements (e.g., Ti and Zr) indicate the presence of rutile and zircon, respectively, which were not dissolved in the ICP-MS preparation. For this reason, Ti, Nb, Ta, Zr, and Hf determined by ICP-MS are not reported. Agreement in Y measured by both techniques demonstrates that the undissolved zircon had < 5% effect on the HREE concentrations determined by ICP-MS.  $^{40}\text{Ar}/^{39}\text{Ar}$  ages of biotite from two xenoliths were measured at Stanford University using analytical techniques detailed in Hacker *et al.* (1996).

## **XENOLITH DESCRIPTIONS**

The xenoliths are as much as 20–30 centimeters in diameter (granulites reach 50 cm), foliated, and contain mm-size minerals; some are composite xenoliths composed of more than one rock type (Table 1; Figure 2). Five types of xenolith were studied in detail: sanidine eclogites, felsic granulites, mafic eclogites, glimmerite, and a phlogopite-garnet websterite. The phlogopite-garnet websterite is picritic in composition, contains orthopyroxene, clinopyroxene, garnet, phlogopite, pyrrhotite and apatite, and is probably of crustal origin based on mineral  $\delta^{18}\text{O}$  values of 6.6–7.1; it is discussed in a separate

publication (Luffi *et al.*, in preparation). The glimmerite, which consists of phlogopite, clinopyroxene, and sanidine, may be metasomatized mantle, but all the rest of the xenoliths that we studied are unambiguously crustal and bear mineral assemblages indicative of ultrahigh temperatures and near-ultrahigh pressures. The mafic eclogites consist of omphacite, garnet and trace rutile and apatite, plus relict amphibole, plagioclase and biotite as garnet inclusions, whereas the sanidine eclogites include the above phases plus sanidine, kyanite, quartz, and minor relict plagioclase. The felsic granulites contain garnet, kyanite, quartz, and alkali feldspar, with minor graphite and rutile. All contain trace zircon and monazite.

Interpreting the histories of the xenoliths depends, in part, on the relative rates of xenolith ascent, thermal conduction and mineral reaction. Spera (1984) calculated ascent rates of  $\sim 0.1\text{--}3$  m/s for alkali basalts bearing cm–dm scale xenoliths with densities of  $3.3\text{ g/cm}^3$ . Such ascent rates carry xenoliths to the surface from depths of 50–100 km in periods of 5–300 hr. Some of the Pamir xenoliths have even higher densities (see below), implying more rapid ascent and shorter transport time. The characteristic thermal diffusion distance for a sphere with thermal diffusivity  $10^{-6}\text{ m/s}^2$  is 0.2–1.8 m for periods of 5–300 hr (Carslaw & Jaeger 1959), implying that the Pamir xenoliths were heated significantly by the magma during transport to the surface. Rates of grain-boundary chemical diffusion in silicates are considerably slower, however, with  $\sim 10\text{--}20\text{ }\mu\text{m}$  thick grain-boundary coronae developing between silicates (e.g., Yund 1997; Milke *et al.* 2001) in 25–50 hr experiments at 1000–1100°C in the presence of an H<sub>2</sub>O-rich fluid. Rates of Fe and Mg volume diffusion in garnet (Ganguly *et al.* 1998) and clinopyroxene (Dimanov & Sautter 2000) are among the slowest phenomena of interest, and imply

diffusive lengthscales of no more than 1  $\mu\text{m}$  over the same timeframe at 1100°C. Na-K interdiffusion in alkali feldspar is 1–2 order(s) of magnitude faster (Christoffersen *et al.* 1983). Thus, the effects of entrainment and transport of the Pamir xenoliths within the host magma are expected to be limited to fracturing, melting, growth of tens-of-micron thick grain-boundary coronae, K-feldspar zoning at the scale of tens-of-microns, and garnet Fe–Mg zoning on the micron scale.

The xenoliths do display textural and chemical changes at these scales resulting from interaction with magma or fluids both before and during eruption. Those changes that *may* have occurred before eruption, based on the grain size of the reaction products and the equilibrated appearance of the textures include:

- i) the decomposition and recrystallization of phlogopite and the growth of sanidine + oxide minerals  $\pm$  glass (Figure 2a, 2b); and
- ii) the crystallization of K-feldspar and carbonate spherules (Figure 2c).

Both of these textures could in principle have formed by reaction with an externally derived magma, but we argue below that the K-feldspar formed from *in situ* melting.

Textural and chemical changes that probably occurred during—or soon before—eruption include:

- i) symplectic breakdown of omphacite in the presence of melt to low-Na clinopyroxene + plagioclase  $\pm$  melt and amphibole + plagioclase (Figure 2b–e, 2j);
- ii) breakdown of kyanite to corundum + quartz and spinel + feldspar symplectite (Figure 2c).

- iii) glass, K-feldspar, and carbonate minerals formed from melt intruded along grain boundaries and along curved transgranular cracks (Figure 2d–h);
- iv) replacement of garnet rims in contact with melt by biotite + K-feldspar symplectite and spinel + K-feldspar + quartz in felsic granulites and mafic eclogites and by amphibole + spinel in sanidine eclogites (Figure 2e, 2g);
- v) growth of micron-scale, bladed K-feldspar grains from interaction of melt with existing alkali feldspar (in felsic granulites and sanidine eclogites);
- vi) potassium enrichment of alkali feldspar rims due to melt infiltration (in felsic granulites and sanidine eclogites); and
- vii) sodium enrichment of alkali feldspar due to breakdown of omphacite (in sanidine eclogites and mafic eclogites).

The sanidine eclogite xenoliths underwent the most alteration, suffering almost all of the effects described above. The mafic eclogite sample is characterized only by biotite dehydration-melting reactions and melt intrusion along grain boundaries and cracks (Figure 2l). The felsic granulite xenoliths are affected only at their margins and along a few grain boundaries and cracks (Figure 2g, 2h).

## **PETROGRAPHY, MINERAL COMPOSITIONS, BULK ROCK COMPOSITIONS**

Sanidine–biotite eclogite **337A** is a heterogeneous rock with garnet + clinopyroxene knots wrapped by biotite + sanidine rich zones (Figure 2b, 2h, 2l). A foliation defined by elongate biotite plus some clinopyroxene and sanidine is folded at the mm to cm scale. Garnet is  $\text{alm}_{54}\text{prp}_{28}\text{grs}_{17}\text{sps}_{01}$  (alm, almandine; prp, pyrope; grs, grossular; sps, spessartine) and shows rimward changes of  $-2$  mol% grossular at constant Mg#



( $=\text{Mg}/(\text{Mg}+\text{Fe})$ ) (Figure 4a). Clinopyroxene have unusually high  $\text{TiO}_2$  contents of 0.8–1.1 wt%, and rare matrix grains show rimward zoning in jadeite ( $\text{NaAlSi}_2\text{O}_6$ ) content from 23 to 40 mol%; grains included within garnet show uniformly high jadeite contents (Figure 4b). Matrix biotite have very high  $\text{TiO}_2$  contents of 6–8 wt% and is more magnesian (Mg#55) than inclusions in garnet (Mg#51). Alkali feldspar grains—weakly zoned in the range  $\text{or}_{57-68}\text{ab}_{31-42}\text{an}_{01-02}$  (or, orthoclase; ab, albite; an, anorthite)—occur in low-strain zones in the rock matrix and as inclusions in garnet. The rock is transected by micron-scale carbonate ( $\text{Ca}_{52}\text{Mg}_{27}\text{Fe}_{21}$ – $\text{Ca}_{52}\text{Mg}_{41}\text{Fe}_{09}$ ) +  $\text{or}_{99}$  alkali feldspar filled fractures (Figures 2h and 4c). Nearly all garnet and omphacite rims have micron-scale symplectites developed as a result of this—although a few garnet–omphacite boundaries and all garnet–inclusion grain boundaries not intersected by carbonate + feldspar veins appear unreacted (Figure 2h). The omphacite coronae are formed of sodic augite and  $\text{An}_{18}$  plagioclase. All matrix biotite have partially decomposed to  $\text{or}_{93}$  alkali feldspar + hercynite–magnetite spinel where in contact with the carbonate + alkali feldspar veins (Figure 2b). Garnet and clinopyroxene decomposition are more advanced in zones rich in decomposed biotite, suggesting that biotite dehydration melting accelerated or triggered garnet and clinopyroxene breakdown. The high  $\text{TiO}_2$  and  $\text{K}_2\text{O}$ , low  $\text{SiO}_2$  and  $\text{Al}_2\text{O}_3$ , and steep REE pattern (Table 3; Figure 3) of 337A are consistent with an alkali basalt (leucite–basanite) protolith.

Eclogite **1154A** has a strong foliation defined by the shape-preferred orientation of omphacite, quartz, rutile, apatite, and slightly oblate garnet grains (Figure 2e, 2g). Garnet are up to 2.2 mm in diameter and have  $\text{alm}_{39}\text{prp}_{39}\text{grs}_{20}\text{sps}_{01}$  cores (Figure 4a) and  $\text{alm}_{39}\text{prp}_{35}\text{grs}_{24}\text{sps}_{01}$  rims. This whole-grain zoning reflects changes of –4 mol% pyrope,

+4 mol% grossular, and –2 Mg#; Fe and Mn are unzoned, and Mg and Ca vary inversely. Omphacite are unzoned, except for sharp, 7% increases in Fe in the outer 15 µm of the grain; omphacite matrix grains and inclusions in garnet share the same composition. Fairly abundant pre-eclogitic inclusions within garnet are magnesian hastingsite  $(\text{Na}_{0.6}\text{K}_{0.3})(\text{Ca}_{1.7}\text{Na}_{0.3})(\text{Mg}_{1.8-2.6}\text{Fe}_{1.7-2.3}\text{Al}_{0.6})(\text{Al}_{1.9}\text{Si}_{6.1})\text{O}_{22}(\text{OH}_{1.0-2.0}\text{F}_{0.0-1.0})$ , plagioclase zoned from An<sub>18</sub> cores to An<sub>36</sub> rims, biotite with 3 wt% TiO<sub>2</sub>, quartz, and apatite. Micron-scale veins filled by carbonate and alkali feldspar transect garnet grains, and carbonates fill rare grain triple-junction pockets as large as 100 µm (similar to Figure 2f). Garnet are surrounded by ~10-µm wide coronae of subsilicic magnesian hastingsite  $(\text{Na}_{0.5}\text{K}_{0.2})(\text{Ca}_{1.4}\text{Na}_{0.6})(\text{Mg}_{2.2}\text{Fe}_{1.5}\text{Al}_{1.3})(\text{Al}_{2.3}\text{Si}_{5.7})\text{O}_{22}(\text{OH}_2) + \text{An}_{20}$  plagioclase. All pyroxene grain boundaries have been penetrated by carbonate veins and formed >10-µm thick symplectites that consumed <10% of the clinopyroxene. Rutile is rimmed by ilmenite where in contact with quenched melt. The calculated bulk composition of this rock is that of a low-K tholeiitic basalt (Table 3; Figure 3).

Sanidine–(kyanite) eclogite **1154B** is a compositionally distinct part of the same xenolith. It has a moderate foliation defined by phase-ratio layering and the shape-preferred orientation of garnet, clinopyroxene, K-feldspar, minor kyanite, and rutile (Figure 2i). Garnet grains as large as 3.5 mm are zoned with decreasing Mg# and increasing Ca from alm<sub>44</sub>prp<sub>34</sub>grs<sub>22</sub>sps<sub>01</sub> to alm<sub>42</sub>prp<sub>29</sub>grs<sub>28</sub>sps<sub>01</sub>; the magnitude and scale of the zoning vary from grain to grain independently of grain size. The garnet grains sport rare inclusions of An<sub>32</sub> plagioclase and hornblende. Omphacite are homogeneous at 44 mol% jadeite and Mg#71. Sanidine have optically visible zoning, from kfs<sub>84</sub>ab<sub>15</sub> to

kfs<sub>74</sub>ab<sub>25</sub>. The bulk composition of 1154B is similar to that of a continental arc tonalite or andesite (Table 3).

Sanidine eclogite **1283** has a moderate foliation defined by elongate patches of clinopyroxene, plus garnet, K-feldspar, rutile, and significant apatite (Figure 2d, 2f, 2k); 1283A and 1283B represent parts of the same xenolith with different clinopyroxene/K-feldspar ratios. Garnet in 1283B are zoned from alm<sub>45</sub>prp<sub>28</sub>grs<sub>26</sub>sp<sub>01</sub> to alm<sub>45</sub>prp<sub>31</sub>grs<sub>24</sub>sp<sub>01</sub>, exhibiting rimward changes of +2 in Mg# and –2 mol% grossular. They bear relatively abundant inclusions of biotite (0.3 wt% TiO<sub>2</sub>), subsilicic ferroan pargasite (Na<sub>0.4</sub>K<sub>0.5</sub>)(Ca<sub>1.9</sub>Na<sub>0.1</sub>)(Mg<sub>2.1</sub>Fe<sub>2.0</sub>Al<sub>0.9</sub>)(Al<sub>2.4</sub>Si<sub>5.6</sub>)O<sub>22</sub>(OH<sub>1.5</sub>F<sub>0.5</sub>), and carbonate (see below). All garnet external grain boundaries—and all garnet inclusion grain boundaries intersected by carbonate-filled veins—have ~10 µm thick symplectite rims. Omphacite vary slightly in jadeite content from 44 to 46 mol% at constant Mg#67; individual grains are replaced 10–100% by micron-scale symplectites of plagioclase, sodic augite, and carbonate. Sanidine of composition kfs<sub>75</sub>ab<sub>24</sub> have micron-scale rims of kfs<sub>99</sub>, are cut by micron-scale carbonate veins, and contain abundant healed fractures. Carbonate constitutes ~2 vol% of the rock and occurs in three textural types: i) distributed thin grain-boundary films and trans-granular cracks (Figure 2f), ii) subrounded inclusions in alkali feldspar (similar to Figure 2c), and iii) polycrystalline inclusions inside garnet (Figure 2k). Most of the carbonate are clustered around the composition Ca<sub>0.55</sub>Mg<sub>0.30</sub>Fe<sub>0.15</sub>CO<sub>3</sub>, but a continuum from Ca<sub>0.54</sub>Mg<sub>0.28</sub>Fe<sub>0.18</sub>CO<sub>3</sub> toward Ca<sub>0.5</sub>Mg<sub>0.5</sub>CO<sub>3</sub>, is clearly separated by a compositional gap from inclusions of pure CaCO<sub>3</sub> (Figure 4). The carbonate inclusions within garnet are anhedral to subhedral and consist of i) euhedral carbonate grains with fine-scale oscillatory zoning visible with

cathodoluminescence and ii) very fine-grained anhedral carbonate grains. Both forms are typically ternary Fe-Mg-Ca carbonate, but some euhedral crystals gave spot analyses of pure  $\text{CaCO}_3$ . Rare barite is associated with the garnet-hosted carbonate inclusions. The bulk compositions of 1283A and 1283B are basaltic to trachybasaltic; 1283B shares an affinity to 1154B in its nearly parallel REE pattern (Table 3; Figure 3).

Sanidine–(kyanite) eclogite **1309** has a granoblastic habit formed by garnet surrounded by clinopyroxene in a sea of K-feldspar, kyanite, quartz, and rutile (Fig 2c, 2j). Minor, but widespread micron-scale transgranular and grain-boundary cracks contain carbonate. Garnet are essentially unzoned with only a minor decrease in Mg# from  $\text{alm}_{46}\text{prp}_{27}\text{grs}_{26}\text{sps}_{01}$  to  $\text{alm}_{47}\text{prp}_{26}\text{grs}_{26}\text{sps}_{01}$ . They contain common inclusions of  $\text{An}_{58-67}$  plagioclase, or  $_{71-82}$  alkali feldspar, quartz, and  $(\text{Mg}_{0.8}\text{Fe}_{1.1}\text{Al}_{0.1})(\text{Al}_{0.2}\text{Si}_{1.8})\text{O}_6$  orthopyroxene, and are surrounded by sodic augite +  $\text{An}_{24}$  plagioclase coronae. Omphacite are homogeneous at 51–52 mol% jadeite and Mg#63–64; all show 20–100% decomposition to symplectites. Sanidine have optically visible zoning from  $\text{kfs}_{73-74}\text{ab}_{25}$  to  $\text{kfs}_{56-68}\text{ab}_{31-43}$ . Some kyanite are surrounded by micron-scale coronae composed of corundum + quartz (Figure 2c). The bulk composition of 1309 is that of an arc tonalite or andesite, similar to 1154B (although it is contaminated by a few vol% of the host lava) (Table 3; Figure 3).

The three pieces of kyanite–garnet granulite xenolith **1503** have granoblastic textures; their foliations are defined by the shape-preferred orientation of quartz, kyanite, alkali feldspar and porphyroblastic garnet and locally by the orientation of graphite flakes and rutile. Garnet from these three samples are near-homogeneous  $\text{alm}_{56}\text{prp}_{39}\text{grs}_{04}\text{sps}_{01}$  with slight rimward increases in grossular of +1 mol% at a constant Mg# of 41. The relic

phengite have Si contents as high as 3.6 atoms per formula unit of 11 oxygen atoms, and high F content ( $X_F = \text{F anions}/2 = 0.35$ ). Alkali feldspar are  $\text{kfs}_{58-70}\text{ab}_{28-40}\text{an}_{02}$ , with rim enrichment to  $\text{kfs}_{99}$  where in contact with alkali-feldspar filled veins. Rare biotite relicts are shielded in garnet grains, whereas phengite and K-feldspar are included in kyanite grains. In contrast to the eclogites, only minor alkali-feldspar  $\text{or}_{99}$  veins and carbonate veins are present in the granulites; healed fractures are absent. Grain-boundary symplectites are minor or absent because of the absence of clinopyroxene. Garnet, kyanite, sanidine, quartz, apatite, monazite, and zircon contain  $\text{CO}_2$ -rich, peraluminous dacitic to rhyodacitic primary glass inclusions with 69.76%  $\text{SiO}_2$ , 0.16%  $\text{TiO}_2$ , 15.74%  $\text{Al}_2\text{O}_3$ , 0.7%  $\text{FeO}^*$ , 0.13%  $\text{MgO}$ , 0.61%  $\text{CaO}$ , 2.05%  $\text{Na}_2\text{O}$ , and 5.73%  $\text{K}_2\text{O}$  and primary  $\text{CO}_2$ -rich fluid inclusions (Chupin *et al.* 2001). The bulk compositions of these rocks are similar to Fe+Mg-rich and Na-poor pelitic schists (Patiño Douce & McCarthy 1998) (Table 3). The major element composition of 1503C is within 20% of Taylor & McLennan's (1985) post-Archean average shale (adjusted to the same silica content to compensate for the higher quartz content of 1503C), except for Na, Ca and P, which are depleted in 1503C.

Glimmerite (or alkali minette) **2014** consists of phlogopite and clinopyroxene with minor apatite, cut by  $\text{or}_{99}$  alkali feldspar veinlets (Figure 2a). Clinopyroxene has <5 mol% jadeite and has completely recrystallized to a clinopyroxene–carbonate symplectite. The phlogopite have 4–5 wt%  $\text{TiO}_2$  and significant F contents; all are recrystallized where in contact with alkali feldspar to more euhedral crystals with slightly higher Si, Mg, Ca and F and slightly lower Al, Ti, Fe, and Na, but are otherwise unchanged.

In summary, all eclogites show intrusion of carbonate and alkali feldspar along fractures that either triggered, enhanced, or accompanied symplectic decomposition of clinopyroxene and garnet. The xenolith compositions span a broad range, from mafic igneous rocks to felsic igneous rocks and metasediments. The association of continental arc magmatic rocks with mature sediments suggests that the bulk of the xenoliths were derived from evolved continental crust.

## **PRESSURE–TEMPERATURE CALCULATIONS**

Pre-eruption temperatures and pressures were determined by thermobarometry (Figures 5–7). Because of the widespread evidence for small-scale disequilibrium in the form of reaction coronas and mineral zoning, we made a careful assessment in each sample of whether rim and core compositions might represent equilibrium, using textural criteria such as the absence of grain-boundary reaction products and compositional criteria such as the magnitude and direction of zoning; this is discussed for each sample on a case-by-case basis below. Generally, the Pamir xenoliths have high-variance assemblages.

Interpreting the mineral zoning in the xenoliths requires knowing the diffusivities of elements in different phases and the operative phase transformations. The simplest rock to consider is the “two-phase” eclogite 1154A, which consists of 59 vol% omphacite, 37% garnet, 2% quartz and other trace phases; some of the 2.2 mm diameter garnet exhibit whole-grain zoning of Mg (–4 mol%) and Ca (+4 mol%) against a homogeneous Fe and Mn background. As noted earlier, the diffusive lengthscale for Fe and Mg volume diffusion at 1100°C over the probable transport time for the xenolith is ~1  $\mu\text{m}$  in garnet (Ganguly *et al.* 1998) and less in clinopyroxene (Dimanov & Sautter 2000)—any larger

scale zoning must therefore be the result of pre-eruption processes. It is improbable that the observed garnet zoning—decreasing Mg (and Mg#) and increasing Ca rimward—could have developed solely through temperature-dependent Fe–Mg exchange with the omphacite, because Fe and Mg have equal charge and do not require compensation by more slowly diffusing Ca (Chakraborty & Ganguly 1992). Alternatively, the garnet zoning could reflect net-transfer reactions among garnet, omphacite and other phases (e.g., melt). This would require an increasing jadeite content in the omphacite to compensate for the loss of Ca from the omphacite to the garnet. The jadeite content of the omphacite cannot change, however, unless another Na-bearing phase exists in the rock. We therefore conclude that the Ca zoning in the garnet reflects consumption of former plagioclase or melt, and that the Mg zoning may reflect simple charge compensation (Mg diffuses more slowly than Fe, Chakraborty & Ganguly 1992); the fact that Mg# decreases rimward in garnet suggests that temperature was declining during the compression-induced net-transfer reactions that pumped Ca into garnet. We ascribe the preservation of this zoning plus the presence of low-pressure inclusions in some rocks to shielding within garnet and to the generally slow reaction rates that are likely to have prevailed in these chiefly anhydrous rocks.

Three types of reaction prove the most valuable for thermobarometry of these rocks: i) Fe–Mg exchange between garnet and clinopyroxene; ii) net-transfer equilibria with positive PT slopes; and iii) net-transfer equilibria with negative PT slopes. These reactions intersect within uncertainty for individual samples (Figure 6). Because of the textural and chemical evidence that mineral rims underwent reaction with the melt,

pressures and temperatures were calculated from mineral compositions interior to the rim zoning.

We calculated the positions of the Fe–Mg exchange equilibrium between garnet and clinopyroxene using three recent calibrations: THERMOCALC (Powell & Holland 1988), Krogh Ravna (2000), henceforth K00, and Ganguly *et al.* (1996), henceforth GCT96. Figure 5 shows that agreement among the three calibrations is not excellent. Both THERMOCALC and GCT96 indicate temperatures ~100°C hotter than K00 at the cooler end of the scale, and, whereas agreement between GCT96 and K00 is excellent around 1100°C, THERMOCALC gives temperatures that are ~150–200°C hotter. To be conservative at the hotter end of the temperature scale, we use the GCT96 and K00 temperatures. These reactions have steep Clapeyron slopes, such that changing the assumed pressure by 0.5 GPa changes the apparent temperature by <45°C (Fig. 5).

Net-transfer reactions with positive slopes that are applicable to these rocks include the albite = jadeite + quartz, plus the less well characterized reaction garnet = Ca-tschermak component in clinopyroxene + clinopyroxene (CaTs). We calculated the position of the latter reaction using THERMOCALC and PTGIBBS (Brandelik & Massonne 2004) with the garnet solution models of Ganguly & Saxena (1984), Berman (1990) and Massonne (1995) and the *C2/c* clinopyroxene solution models of AX (<http://www.esc.cam.ac.uk/astaff/holland/ax.html>) and PTGIBBS, which explicitly consider jadeite, acmite, and Ca-tschermak components. The different solution models for clinopyroxene yield calculated CaTs-based pressures that differ by >0.5 GPa, much greater than the 0.1 GPa uncertainty induced by 10% variation in CaTs activity. We calculated plagioclase activities using the average of models 3 and 4 of Holland & Powell



(1992) (using  $X_{an} = 1 - Na - K$  and  $X_{ab} = Na$ ), incrementing the uncertainties of the activities to include the range in activities encompassed by the models. We calculated alkali feldspar activities using an average of the two solution models of Hovis *et al.* (1991) for disordered alkali feldspar. Five percent uncertainty in the jadeite activity in clinopyroxene translates into  $\pm 0.3$  kbar relative deviation; following Tropper *et al.* (1999), we assigned an absolute uncertainty of  $\pm 0.9$  kbar ( $1\sigma$ ) to the position of the albite = jadeite + quartz equilibrium calculated with these activities. In kyanite-bearing samples we used the 1 pyrope + 1 grossular + 2 quartz = 3 diopside + 2 kyanite (GCKQ) net-transfer reaction, which has a negative PT slope; we used the method of Ravna & Terry (2004), based on the garnet activity model of Ganguly *et al.* (1996), the clinopyroxene activity model of Holland (1990), and the Holland & Powell (1998) database. These equilibria were supplemented with reactions calculated by THERMOCALC when possible.

Sanidine–kyanite eclogite **1154B** has a lower variance mineral assemblage, such that pressure and temperature can be estimated from three reactions: Fe–Mg partitioning between garnet and clinopyroxene, the albite breakdown reaction using the activity of albite in sanidine (Hovis *et al.* 1991), and the pyrope + grossular + quartz = diopside + kyanite net-transfer reaction (Figure 6). Intersections among these equilibria span 24.7–28.0 kbar and 1015–1060°C.

Pressure and temperature can be estimated for the more mafic piece of the same xenolith, **1154A**, by using the intersection of the garnet–clinopyroxene Fe–Mg exchange reaction and the CaTs component in omphacite in equilibrium with garnet (Figure 6). Depending on the calibration chosen, intersections among these equilibria range from a minimum of ~22.5 kbar and 1010°C to a maximum of 28.5 kbar and 1050°C. A

minimum pressure of ~21 kbar is given by the albite = jadeite + quartz reaction, assuming—in the absence of matrix feldspar—that  $a_{ab} = 1$ .

Pressure and temperature can be estimated for sanidine xenolith **1283B** from intersection of the garnet–clinopyroxene Fe–Mg exchange reaction and the albite = jadeite + quartz reaction, using  $a_{ab}$  for sanidine (Hovis *et al.* 1991) (Figure 6). The intersections are at 1100°C [K00] and 28.5 kbar and 1130°C [GCT96] and 29.2 kbar (Figure 6). Fe–Mg partitioning between garnet and biotite indicates temperatures ~35°C hotter, using THERMOCALC.

Sanidine–kyanite eclogite **1309** has an identical mineral assemblage to 1154B and permits application of the same thermometers and barometers (Figure 6). Intersections among the Fe–Mg exchange, albite-breakdown, and GCKQ reactions span a relatively narrow range of 26.5–30.5 kbar and 1035–1090°C.

The pressure–temperature conditions of the mineral assemblage in kyanite–garnet granulite **1503** are difficult to constrain using thermobarometry because of the high variance assemblage. Fe–Mg partitioning between garnet and biotite inclusions in 1503B indicates temperatures of ~1080°C, but this is probably a maximum because Fe–Mg exchange between the rare and tiny biotite inclusions and their host garnet certainly continued after entrapment. We can, however, exploit the experiments of Patiño Douce & McCarthy (1998) on a muscovite schist to place constraints on the equilibration conditions. Those experiments demonstrate that the presence of garnet + K-feldspar + kyanite + quartz and the absence of omphacite, biotite, muscovite, and plagioclase, implies temperatures between 1025°C and 1060°C at 2.1 GPa (Figure 7). They further suggest equilibration pressures between ~2.1 and 3.0 GPa.

Sanidine–biotite eclogite **337A** yields different results from the other samples. Fe–Mg partitioning between garnet and clinopyroxene indicates temperatures of 720–750°C [K00] or 865–880°C [GCT96] for an assumed pressure interval of 20–25 kbar. Fe–Mg exchange between garnet and biotite rims (Ganguly *et al.* 1996) indicates slightly higher temperatures than GCT96 (900–925°C), regardless of whether an ideal or nonideal Al–Ti mixing model is chosen for biotite (Patiño Douce *et al.* 1993). Because both plagioclase and quartz are absent, pressure cannot be determined quantitatively from the mineral assemblage. However, if we assume that all the xenoliths were sampled along a single geotherm, we can estimate pressure from the intersection of that geotherm with the Fe–Mg garnet–clinopyroxene exchange equilibrium. Figure 7 shows that two geotherms for the United Kingdom and the eastern United States from Sclater *et al.* (1980) pass through the PT conditions of the xenoliths. These geotherms intersect the Fe–Mg garnet–clinopyroxene exchange equilibrium for 337A at ~2.0–2.5 GPa (Figure 7)

## ORIGIN AND EVOLUTION OF THE XENOLITHS

This section marshals textural, paragenetic and mineral compositional evidence to assess the origin and evolution of the Pamir xenoliths. The xenoliths are the result of i) high-pressure dehydration melting that produced a dense, refractory residuum and a K-rich silicate liquid; ii) carbonate metasomatism; and, possibly, iii) potassic metasomatism that caused phlogopite and sanidine crystallization.

## **Hydrous eclogite**

If the protolith of 337A was an alkali basalt or a equivalent plutonic rock (biotite–nepheline monzodiorite–diorite), the presence of abundant biotite and sanidine could simply reflect the bulk composition of the rock. Alternatively, the biotite and/or sanidine might have been introduced to the rock as a melt or fluid. The presence of sanidine and biotite inclusions in garnet requires that such introduction predated garnet growth. The lower calculated equilibration temperature and the lower inferred equilibration pressure suggest that this xenolith was extracted from a different depth in the lithosphere and has a different history than the other xenoliths.

## **Anhydrous eclogites**

The bulk chemical compositions of samples 1154B and 1309 resemble those of quartz monzonites or biotite granodiorites to calc-alkaline tonalites. The nominal bulk compositions of mafic eclogites 1154A, 1283A, and 1283B suggest derivation from basaltic protoliths. However, the bulk compositions are so similar to the residua produced by Patiño Douce & McCarthy (1998) during experimental partial melting of calc-alkaline tonalite (Figure 8), that they are more likely residua derived from partial melting of typical continental-margin magmatic arc rocks. According to Patiño Douce & McCarthy (1998), dehydration melting of amphibole–biotite tonalites at 19–24 kbar and  $T > 950^{\circ}\text{C}$  produces a solid residuum of garnet + omphacite + sanidine + quartz—similar to the sanidine eclogite xenoliths from the Pamir. The amphibole and plagioclase preserved in garnet cores are compatible with this interpretation. The only difference, the presence of kyanite in 1154B and 1309, suggests that the protoliths could have been richer in  $\text{Al}_2\text{O}_3$ . The REE patterns of these rocks suggest melt loss in the presence of garnet; such a

process is permissible if the protoliths had steep REE patterns, typical of Andean or Sierran intermediate arc magmas (Figure 3), which have major element abundances broadly similar to these xenoliths.

The thin grain-boundary films of carbonate in 1283B are likely the result of late-stage intrusion of the xenolith by a carbonate-rich fluid. The rounded inclusions within alkali feldspar crystals (Figure 2c) might represent crystallization of sanidine + carbonate from a carbonate-rich alkalic melt (Lee & Wyllie 1998). The polycrystalline carbonate inclusions inside garnet have fine-scale compositional zoning and are euhedral (Figure 2k). Because such fine-scale zoning should have been instantly erased by diffusion at these elevated temperatures, the carbonates must have crystallized during or soon before eruption and are presumably physically connected to veins outside the garnet.

### **Kyanite–garnet granulites**

The bulk compositions, mineralogies, and glass inclusions of samples 1503A, 1503B, and 1503C, suggest that these rocks are residua of high-pressure melting of two-mica pelitic protoliths. Rare biotite inclusions in garnet, and phengite and alkali feldspar inclusions in kyanite suggest a feldspathic two-mica protolith. The mineral assemblage, garnet + kyanite + sanidine + quartz, is identical to that observed by Castro *et al.* (2000) to form from experimental dehydration melting of two-mica pelites at elevated pressures. These xenoliths cannot represent quenched high-pressure melts, as they have SiO<sub>2</sub> and Al<sub>2</sub>O<sub>3</sub> contents that are granitic (*sensu lato*), but the concentrations of alkali elements and MgO + FeO are opposite to that expected in granitic melts. The REE pattern of 1503C, with its HREE enrichment and LREE depletion relative to average shale (Figure 3c), is

quantitatively consistent with > 40% removal of a melt with a very steep REE pattern—as expected for a melt in equilibrium with garnet. While garnet was likely present during a substantial part of this granulite’s P-T-t path, it is likely that the REE pattern of the rock reflects melting with garnet in the residue near the peak P-T conditions. The calculated REE pattern slightly differs from those of glass inclusions found in quartz from similar granulite xenoliths from the Pamir (Chupin *et al.* 2001). The glass inclusions have similar HREE, but higher LREE concentrations; these could represent an earlier melt fraction. Alternatively, the difference could be explained by slightly different bulk compositions or melting histories.

### **Glimmerite**

Glimmerite 2014 is interpreted to represent the result of interaction between a H<sub>2</sub>O-rich potassic melt (or fluid) and a ferro-magnesian host rock. The apparent chemical equilibrium between sanidine and phlogopite, plus the absence of mafic neoblasts along the biotite/feldspar interfaces makes it clear that the sanidine was not produced by dehydration melting of the biotite. Such potassic melts or fluids might be derived from the asthenosphere (Menzies *et al.* 1987; Gregoire *et al.* 2002) or by the high-pressure breakdown of fluorinated biotite in felsic granulites (Becker *et al.* 1999); the absence of mantle xenoliths in this suite implies the latter. It is also possible that 2014, with its 80% modal biotite, represents a cumulate crystallized from a K-rich melt. The very steep REE pattern requires derivation from a source containing garnet.

## **ERUPTION AGE**

Biotite from xenoliths 337A and 2014 were dated via stepwise degassing in a resistance furnace at Stanford University. The samples yielded slightly different ages of  $11.52 \pm 0.22$  Ma ( $2\sigma$ ) and  $11.17 \pm 0.14$  Ma, respectively (Figure 9). As both samples were at temperatures well above Ar retention in biotite prior to eruption, these ages are unambiguously eruption ages. The differences between the apparent ages of the two xenoliths might indicate slightly different eruption times or may be geologically meaningless.

## **DEEP CRUST BENEATH THE SOUTHEASTERN PAMIR**

The thermobarometric calculations and mineral parageneses detailed above suggest that most of the xenoliths investigated equilibrated at high pressures and temperatures,  $P$  25–28 kbar and  $T = 1000$ – $1100^\circ\text{C}$ . The rocks span the entire range of probable crustal compositions—basaltic to tonalitic to pelitic—in the grossest sense. We have interpreted the textures and minerals within the xenoliths to be the result of partial melting and enrichment metasomatism at high pressure; most of the minerals present represent residua, while others, specifically sanidine and biotite, in some samples represent quenched melt or fluid derived either locally or introduced from a distance. These xenoliths were carried to the surface in a volatile-rich magma at  $\sim 11$  Ma, which may have formed by melting of enriched subcontinental upper mantle (e.g., Turner *et al.* 1996; Miller *et al.* 1999)—as has been suggested for the Neogene granitoids of the south Karakoram (Mahéo *et al.* 2002).

Laser ablation MC-ICP-MS dating of zircons was performed on two of these xenoliths by Ducea *et al.* (2003). Sanidine–(kyanite) eclogite 1309, here interpreted as a calc-alkaline monzonite to tonalite originating from dehydration melting of amphibolite-biotite tonalite, underwent igneous crystallization at ~63–88 Ma and contains inherited zircons with ages of ~132 Ma, ~195 Ma, and ~250 Ma. The pelitic protolith of kyanite–garnet granulite 1503A was either deposited after ~57 Ma or underwent high-grade zircon growth at ~57–84 Ma; older zircons are 146–170 Ma, 412–465 Ma, 890 Ma and 1.4 Ga. The early Paleozoic and Precambrian zircon ages prove that the xenoliths were derived from Gondwanan crust (e.g., DeCelles *et al.* 2000); the Mesozoic ages preclude derivation of the xenoliths from Indian crust, as India does not contain magmatic rocks of Mesozoic age (with the exception of minor rift-related alkalic volcanism, Hodges 2000). The zircon ages are compatible with derivation of the xenoliths from crust of the type presently exposed in a ~300 km wide belt in the Karakoram–Kohistan–Ladakh and Hindu Kush–southern Pamir blocks (e.g., Gaetani 1996; Fraser *et al.* 2001; Schwab *et al.* 2004); these blocks are Gondwanan, and contain Jurassic to Late Cretaceous plutons produced by prolonged northward subduction of Tethys. The southern Pamir contain granodiorite and two-mica monzogranite with Proterozoic to Cretaceous zircon ages (Schwab *et al.* 2004) identical to those found in the xenoliths (Ducea *et al.* 2003). The Kohistan arc, especially its southern, deeply exhumed part contains variously metamorphosed calc-alkaline to tholeiitic gabbros, diorites, and granodiorites with ages of 82–99 Ma (e.g., Searle 1991; Schaltegger *et al.* 2002). The Karakoram and Hindu Kush also include voluminous siliciclastic rocks (mostly shales) of various metamorphic grades that underwent several high-strain thickening events before and after the India–Asia collision



(e.g., Gaetani 1996; Zanchi & Gritti 1996; Fraser *et al.* 2001). Granulite-facies, Barrovian metamorphism in the Karakoram block is pre-37 Ma, and 25 Ma to Recent (Fraser *et al.* 2001; Mahéo *et al.* 2002). This is similar to the prograde high-temperature metamorphism of xenolith 1503A, which bears 50 and 34 Ma monazites and ~15 Ma zircon rims (Ducea *et al.* 2003).

Is it possible that the carbonatites—traditionally considered to be products of deep melting of mantle rocks under high CO<sub>2</sub> fugacities—in the Pamir xenoliths might have been produced by melting/decarbonation of sedimentary carbonates? Marble is known from within the Kohistan arc itself, but is very rare. Aptian–Albian limestone blocks in the Shyok mélange along the northern rim of the Kohistan arc were likely derived from the Yasin Group, which overlies the Chat volcanic sequence in the Kohistan arc south of the suture. The eastern Shyok suture zone also has small occurrences of Eocene foraminiferal limestone. The Karakoram block exposes thick Devonian, Triassic, uppermost Jurassic and Lower Cretaceous carbonate sections in the Hejmand, northern Karakoram, SE Pamir, and Saksgam areas.

## **DEEP CRUST BENEATH THE PAMIR AND TIBET**

These Pamir xenoliths were erupted at ~11 Ma from depths of ~90–100 km (pressure converted to depth using the global density profile of Christensen & Mooney 1995). The eruption depth was 20–30 km deeper than the ~70 km thickness of the present-day Pamir crust (Burtman & Molnar 1993; Mellors *et al.* 1995), suggesting that the xenoliths were derived from a subducted crustal slab or from foundered lower crust. The absence of mantle xenoliths implies that the eruption pathway remained entirely within the crust.

The similarities between the compositions and ages of the xenoliths and exposed crustal rocks in the Pamir suggest that part of a Late Cretaceous arc built on Gondwanan continental crust (likely the Kohistan–Ladakh–Gangdese arc with its Lhasa block basement) was subducted northward beneath the Pamir—either following subduction of a small trapped ocean basin (Burtman & Molnar 1993) or driven by intracontinental shortening (Figure 11a). The temperatures, which are higher than expected for subduction, based on ultrahigh-pressure terranes, may have resulted from conductive heating following cessation of subduction or simply from slow subduction. Alternatively, pieces of the lower crust of this same arc may have been pulled into the mantle by a density instability (Figure 11b) (e.g., Jull & Kelemen 2001)—if the lower crust were dominated by eclogite rather than garnet granulite. The zircon ages of the xenoliths require this subduction/foundering to be younger than 57 Ma. If intracontinental subduction is the cause, it may have occurred along any one of the sutures within or south of the southern Pamir: the early Cenozoic Indus–Yarlung suture, the Shyok suture where the Kohistan–Ladakh arc accreted to Asia in the Late Cretaceous (e.g., Schaltegger *et al.* 2002), or the Tirich Mir fault zone which has existed since the pre-mid-Cretaceous (Hildebrand *et al.* 2001). It may have occurred during the early stages of the India–Asia collision (dated at ~54 Ma in the western Himalaya, Searle *et al.* 1997) and may have produced the 50–34 Ma high-grade metamorphism of the xenoliths. Alternatively, the monazite and zircon rim growth could have occurred during high-grade metamorphism at crustal depths and the subduction could be younger than 50, 34, or 15 Ma. If foundering of the lower crust is the cause, it should not be much older than the eruption age of the

xenoliths because of the rapid timescale of assimilation within the asthenosphere (~10 Myr for a body of 10-km radius).

Subducted continental slabs that detach from the surrounding oceanic lithosphere that is dragging them into the mantle are expected to rise at least to Moho depths because of their positive buoyancy (e.g., Chemenda *et al.* 2000; Walsh & Hacker 2004). It is probable, therefore, that the slab of Pamir continental crust that we infer was subducted or foundered to near-UHP depths in the Eocene(?)–Miocene subsequently rose to form (or add to) the lower crust of the Pamir. Schwab *et al.* (2004) suggested that the lower crust of the Pamir as far north as the central Pamir Qiangtang block (and likely the Karakoram and the Hindu Kush) is made of Gondwanan crust. This is strikingly similar to the southern half of Tibet, for which Murphy *et al.* (1997) suggested that the Lhasa block with its Jurassic to early Cenozoic Gangdese-arc rocks was thrust northward beneath Asia as far north as the central Qiangtang during the Cretaceous and early Tertiary.

Our xenolith studies in the southeastern Pamir (this study) and central Tibet (Hacker *et al.* 2000) support an emerging picture of the first-order crustal structure of the Pamir and Tibet (Fig. 1c) (Schwab *et al.* 2004). The xenoliths of the southeastern Pamir indicate that the lower crust south of the central Qiangtang block likely is tonalitic–granodioritic, reflecting long-lived and intense subduction, arc formation, and Cretaceous–Cenozoic underthrusting of these arc segments together with their Gondwanan host rocks beneath Asia as far north as the central Qiangtang block. In contrast, dominantly metasedimentary xenoliths were erupted in the northern Qiangtang (Hacker *et al.* 2000), Songpan–Ganze flysch (Deng *et al.* 1996), and southernmost Kunlun belts (Jolivet *et al.* 2003) (Fig. 1c),

suggesting that the northern Pamir and northern Tibet both have a dominantly sedimentary lower crust formed from subducted Triassic Songpan–Ganze accretionary wedge rocks (Kapp *et al.* 2003). This first-order, two-part crustal structure is likely the cause of the north-south variation observed in geophysical studies: for example, Owens & Zandt (1997) reported that Tibet is characterized by 70-km-thick, slow-P-wave, average-Poisson’s-ratio crust in the south and 55-km-thick, fast-P-wave, high-Poisson’s ratio crust in the north.

## **PHYSICAL PROPERTIES**

Subduction of continental crust beneath the Pamir is one of the types of tectonic settings in which ultrahigh-pressure rocks—supracrustal rocks exhumed from depths exceeding 100 km—may be created (Searle *et al.* 2001). While some ultrahigh-pressure terranes appear to have undergone melting at ultrahigh pressures—e.g., Kokchetav and Erzgebirge (Massonne 2003)—such terranes are strongly modified during their ascent to the surface. The Pamir xenoliths thus afford a unique probe into ultrahigh-pressure tectonics and the chemical and physical processing that takes place in such environments. The temperatures inferred for the Pamir xenoliths are ~200°C hotter than inferred for most ultrahigh-pressure terranes, suggesting that they are sampling a regime not normally experienced or preserved.

What are the geodynamic effects of dehydration melting and metasomatism at ultrahigh-pressure conditions? How does such petrologic processing at ultrahigh pressures affect our view of subduction zones and the lower continental crust obtained through seismological study? These questions can be addressed in preliminary fashion by

calculating the densities and seismic wave speeds of the xenoliths at the high pressures and temperatures at which these xenoliths equilibrated (Table 4). Figure 11 compares these with calculated values for mantle rocks at the same pressures and temperatures. Not surprisingly, the former pelitic rocks are the least dense. In fact, most of the xenoliths are less dense than the surrounding mantle and would have been positively buoyant with respect to the mantle. However, two of the xenoliths, mafic eclogites 1154A and 1283A, are significantly more dense than the surrounding mantle, were negatively buoyant, and would have sunk within the mantle given a low enough mantle viscosity (we do not detect evidence of this sinking in the xenoliths). Moreover, while the bulk of the xenoliths have calculated seismic wave speeds that are significantly slower than mantle rocks, these same two mafic eclogite xenoliths have calculated wave speeds that are indistinguishable from the mantle, reinforcing the notion that wave speeds cannot be used to detect the presence of mafic crustal rocks sequestered in the mantle.

The overall effect of dehydration melting—if the melt leaves the rock—is to produce a denser and seismically faster residuum (Figure 11). In the Pamir xenoliths, this refining process increased densities and wave speeds by ~10%, but in the more felsic xenoliths it did not produce rocks that are as dense and seismically fast as lherzolite and harzburgite. Thus, even at near-ultrahigh pressures and extreme temperatures, felsic to intermediate continental crustal material is still differentiable from the mantle using seismic waves. While one might be tempted to conclude that P-wave speeds of >7.5 km/s in the deep parts of orogenic belts are “lower crustal” or mafic in composition, these xenoliths demonstrate that such physical properties also characterize “upper crustal” felsic to intermediate lithologies that have been devolatilized by dehydration melting. The high-

pressure melting of the felsic/intermediate xenoliths (1154B, 1283B, 1309) also did not increase their densities enough to cause the xenoliths to be negatively buoyant with respect to the mantle (Figure 11). In contrast, the residual mafic rocks (1154A, 1283A) are denser than the mantle by virtue of their garnet + clinopyroxene mineralogy; such rocks could sink into a low-viscosity asthenosphere. The most dramatic and interesting effects are, however, produced by enrichment metasomatism—expressed most eloquently in 2014. For such rocks, the addition of hydrous potassic melt to form sanidine and biotite produces a big enough reduction in density that they become buoyant with respect to the mantle; this means that enrichment metasomatism provides a mechanism whereby even eclogite and ultramafic rocks can be returned to the Moho. Fluid-driven metasomatism also produces rocks that are seismically slow and have high  $V_P/V_S$  ratios because of the abundance of phlogopite and sanidine. The seismic properties of such rocks—particularly their high Poisson's ratios (Table 5) means that they could be mistaken in seismological studies for the presence of partial melt.

## CONCLUSIONS

Xenoliths erupted at 11 Ma in the southeastern Pamir suggest that Gondwanan crust overprinted by a Cretaceous magmatic arc on the southern margin of Eurasia was subducted or foundered to near-ultrahigh-pressure depths of 90–100 km beneath Eurasia during Eocene(?)–Miocene intracontinental convergence. Combined with Tibetan xenoliths and surface exposures, these xenoliths suggest that the Pamir and Tibet share similar crustal architectures—a southern lower crust composed of Gondwanan crust overprinted by a Cretaceous magmatic arc and a northern lower crust composed of clastic

sedimentary rocks—produced by parallel tectonic evolutions. The Pamir crust reached temperatures of ~1000–1100°C after dehydration melting, enrichment metasomatism, and melt injection. This processing at extreme temperatures and pressures caused significant changes in physical properties of the deeply buried crust: melting decreased buoyancy whereas melt injection/metasomatism increased buoyancy.

## **ACKNOWLEDGEMENTS**

E.A. Dmitriev gave us this collection of xenoliths. The ms was reviewed by Jane Selverstone, editor Geoffrey Clarke, and an anonymous individual. Jiba Ganguly provided advice and reprints regarding major element diffusivities in garnet and pyroxene. Supported by NSF grant EAR-0003568 to Hacker, and OCE-0137110 to Plank.

## REFERENCES CITED

- Becker, H, Wenzel, T & Volker, F (1999) Geochemistry of glimmerite veins in peridotites from lower Austria - implications for the origin of K-rich magmas in collision zones. *Journal of Petrology* **40**, 315-338.
- Berman, RG (1990) Mixing properties of Ca-Mg-Fe-Mn garnets. *American Mineralogist* **75**, 328–344.
- Brandelik, A & Massonne, H-J (2004) PTGIBBS - an EXCEL Visual Basic program for computing and visualizing thermodynamic functions and equilibria of rock-forming minerals. *Computers and Geosciences* **30**, 909-923.
- Burtman, VS & Molnar, P (1993) Geological and geophysical evidence for deep subduction of continental crust beneath the Pamir. *Geological Society of America Special Paper* **281**, 1-76.
- Carslaw, S & Jaeger, JC (1959) *Conduction of Heat in Solids*. Oxford University Press: New York.
- Castro, A, Corretgé, G, El-Biad, M, El-Hmidi, H, Fernández, C & Patiño-Douce, AE (2000) Experimental constraints on Hercynian anatexis in the Iberian Massif, Spain. *Journal of Petrology* **41**, 1471-1488.
- Chakraborty, S & Ganguly, J (1992) Cation diffusion in aluminosilicate garnets; experimental determination in spessartine-almandine diffusion couples, evaluation of effective binary, diffusion coefficients, and applications. *Contributions to Mineralogy and Petrology* **111**, 74-86.
- Chemenda, AI, Burg, J-P & Mattauer, M (2000) Evolutionary model of the Himalaya–Tibet system: geopoem: based on new modelling, geological and geophysical data. *Earth and Planetary Science Letters* **174**, 397-409.
- Christensen, NI & Mooney, WD (1995) Seismic velocity structure and composition of the continental crust: a global view. *Journal of Geophysical Research* **100**, 9761–9788.
- Christoffersen, R, Yund, RA & Tullis, J (1983) Inter-diffusion of K and Na in alkali feldspars; diffusion couple experiments. *American Mineralogist* **68**, 1126-1133.
- Chupin, VP, Kuzmin, DV & Touret, JLR (2001) High-pressure melt and fluid inclusions in minerals of garnet granulites/eclogites (eastern Pamir). *XVI ECROFI European Current Research On Fluid Inclusions Abstracts, Faculdade de Ciências do Porto, Departamento de Geologia, Memória* **7**, 95–98.



- DeCelles, PG, Gehrels, GE, Quade, J, LaReau, B & Spurlin, M (2000) Tectonic implications of U/Pb zircon ages of the Himalayan orogenic belt in Nepal. *Science* **288**, 497-499.
- Deng, W, Zheng, X & Matsumoto, Y (1996) Petrological characteristics and ages of Cenozoic volcanic rocks from the Hoh Xil Mts., Qinghai Province. *Acta Petrologica et Mineralogica* **15**, 289-297.
- Dimanov, A & Sautter, V (2000) "Average" interdiffusion of (Fe,Mn)-Mg in natural diopside. *European Journal of Mineralogy* **12**, 749-760.
- Dmitriev, EA (1976) *Kainozoiskie kaliyevye schelochnye porody Vostochnogo Pamira [Cenozoic potassium rocks of Eastern Pamir]*. Donish: Dushanbe.
- Ducea, MN, Lutkov, V, Minaev, VT, Hacker, B, Ratschbacher, L, Luffi, P, Schwab, M, Gehrels, GE, McWilliams, M, Vervoort, J & Metcalf, J (2003) Building the Pamirs: the view from the underside. *Geology* **31**, 849-852.
- Fraser, JE, Searle, MP, Parrish, RR & Noble, SR (2001) Chronology of deformation, metamorphism, and magmatism in the southern Karakoram Mountains. *Geological Society of America Bulletin* **113**, 1443-1455.
- Frost, TP (1987) Sample localities, descriptions, major- and trace-element abundances from the Lamarck Granodiorite and associated mafic rocks, eastern Sierra Nevada, California. *U. S. Geological Survey Open File Report* **87-0193**, 38.
- Gaetani, M (1996) The Karakorum block in Central Asia, from Ordovician to Cretaceous. *Sedimentary Geology* **109**, 339-359.
- Ganguly, J, Cheng, W & Chakraborty, S (1998) Cation diffusion in aluminosilicate garnets; experimental determination in pyrope-almandine diffusion couples. *Contributions to Mineralogy and Petrology* **131**, 171-180.
- Ganguly, J, Cheng, W & Tirone, M (1996) Thermodynamics of aluminosilicate garnet solid solution: new experimental data, and optimized model, and thermometric applications. *Contributions to Mineralogy and Petrology* **126**, 137-151.
- Ganguly, J & Saxena, SK (1984) Mixing properties of aluminosilicate garnets; constraints from natural and experimental data, and applications to geothermo-barometry. *American Mineralogist* **69**, 88-97.
- Gregoire, M, Bell, DR & Le Roex, AP (2002) Trace element geochemistry of glimmerite and MARID mantle xenoliths: their relationship to kimberlites and to phlogopite-bearing peridotites revisited. *Contributions to Mineralogy and Petrology* **142**, 603-625.

- Hacker, BR & Abers, GA (2004) Subduction Factory 3. An Excel worksheet and macro for calculating the densities, seismic wave speeds, and H<sub>2</sub>O contents of minerals and rocks at pressure and temperature. *Geochemistry, Geophysics, and Geosystems* **5**, Q01005, doi: 10.1029/2003GC000614.
- Hacker, BR, Abers, GA & Peacock, SM (2003) Subduction Factory 1. Theoretical mineralogy, density, seismic wave speeds, and H<sub>2</sub>O content. *Journal of Geophysical Research* **108**, 10.1029/2001JB001127.
- Hacker, BR, Gnos, E, Ratschbacher, L, Webb, L, Grove, M, McWilliams, M, Jiang, W & Wu, Z (2000) Hot and dry xenoliths from the lower crust of Tibet. *Science* **287**, 2463-2466.
- Hacker, BR, Mosenfelder, JL & Gnos, E (1996) Rapid ophiolite emplacement constrained by geochronology and thermal considerations. *Tectonics* **15**, 1230–1247.
- Hildebrand, PR, Noble, SR, Searle, MP, Waters, DJ & Parrish, RR (2001) Old origin for an active mountain range: Geology and geochronology of the eastern Hindu Kush, Pakistan. *Geological Society of America Bulletin* **113**, 625-639.
- Hodges, KV (2000) Tectonics of the Himalaya and southern Tibet from two perspectives. *Geological Society of America Bulletin* **112**, 324-350.
- Holland, TJB (1990) Activities in omphacitic solid solutions: an application of Landau theory to mixtures. *Contributions to Mineralogy and Petrology* **105**, 446-453.
- Holland, TJB & Powell, R (1992) Plagioclase feldspars: Activity–composition relations based upon Darken's quadratic formalism and Landau theory. *American Mineralogist* **77**, 53–61.
- Holland, TJB & Powell, R (1998) An internally consistent thermodynamic data set for phases of petrological interest. *Journal of Metamorphic Geology* **16**, 309-343.
- Hovis, GL, Delbove, F & Roll-Bose, M (1991) Gibbs energies and entropies of K–Na mixing for alkali feldspars from phase equilibrium data: implications for feldspar solvi and short-range order. *American Mineralogist* **76**, 913–927.
- Hubbard, MS, Grew, ES, Hodges, KV, Yates, MG & Pertsev, NN (1999) Neogene cooling and exhumation of upper-amphibolite-facies 'whiteschists' in the southwest Pamir Mountains, Tajikistan. *Tectonophysics* **305**, 325-337.
- Jolivet, M, Brunel, M, Seward, D, Xu, Z, Yang, J, Malavieille, J, Roger, F, Leyreloup, A, Arnaud, N & Wu, C (2003) Neogene extension and volcanism in the Kunlun fault zone, northern Tibet: new constraints on the age of the Kunlun fault. *Tectonics* **22**, 1051, doi:10.1029/2002TC001460.

Jull, M & Kelemen, PB (2001) On the conditions for lower crustal convective instability. *Journal of Geophysical Research* **106**, 6423–6445.

Kapp, P, Yin, A, Manning, CE, Harrison, TM, Taylor, MH & Ding, L (2003) Tectonic evolution of the early Mesozoic blueschist-bearing Qiangtang metamorphic belt, central Tibet. *Tectonics* **22**, 1043 10.1029/2002TC001383.

Kay, SM, Mpodozis, CM, Ramos, VA & Munizaga, F (1991) Magma source variations for mid-late tertiary magmatic rocks associated with a shallowing subduction zone and a thickening crust in the central andes (28 to 33°S). *Geological Society of America Special Paper* **265**, 113-137.

Kelley, KA, Plank, T, Ludden, JN & Staudigel, H (2003) The composition of altered oceanic crust at ODP sites 801 and 1149. *Geochemistry, Geophysics, and Geosystems* **4**, 10.1029/2002GC000435.

Krogh Ravna, E (2000) The garnet–clinopyroxene Fe<sup>2+</sup>–Mg geothermometer: an updated calibration. *Journal of Metamorphic Geology* **18**, 211–219.

Lee, WJ & Wyllie, PJ (1998) Processes of Crustal Carbonatite Formation by Liquid Immiscibility and Differentiation, elucidated by Model Systems. *Journal of Petrology* **39**, 2005–2013.

Lutkov, VS (2003) Petrochemical evolution and genesis of potassium pyroxenite–eclogite–granulite association in the mantle and crustal xenoliths from Neogene fergusites of South Pamir, Tajikistan. *Geochimica* **3**, 254-265.

Mahéo, G, Guillot, S, Blichert-Toft, J, Rolland, Y & Pêcher, A (2002) A slab breakoff model for the Neogene thermal evolution of South Karakoram and South Tibet. *Earth and Planetary Science Letters* **195**, 45-58.

Massonne, H-J (1995) Experimental and petrogenetic study of UHPM. In: COLEMAN, R & WANG, X (eds.) *Ultrahigh Pressure Metamorphism*. pp. 33-95. Cambridge University Press.

Massonne, H-J (2003) A comparison of the evolution of diamondiferous quartz-rich rocks from the Saxonian Erzgebirge and the Kokchetav Massif: are so-called diamondiferous gneisses magmatic rocks? *Earth and Planetary Science Letters* **216**, 347–364.

Mellors, RJ, Pavlis, GL, Hamburger, MW, Al-Shukri, HJ & Lukk, AA (1995) Evidence for a high-velocity slab associated with the Hindu Kush seismic zone. *Journal of Geophysical Research* **100**, 4067-4078.

Menzies, MA, Rogers, N, Tindle, A & Hawkesworth, CJ (1987) Metasomatic and enrichment processes in lithospheric peridotites, an effect of lithosphere–asthenosphere

interaction. In: Menzies, MA & Hawkesworth, CJ (eds.) *Mantle Metasomatism*. pp. 313–363. Academic Press: London.

Milke, R, Wiedenbeck, M & Heinrich, W (2001) Grain boundary diffusion of Si, Mg, and O in enstatite reaction rims: a SIMS study using isotopically doped reactants. *Contributions to Mineralogy and Petrology* **142**, 15–26.

Miller, C, Schuster, R, Klötzli, U, Mair, V, Frank, W & Purtscheller, F (1999) Post-collisional potassic and ultrapotassic magmatism in SW Tibet: Geochemical and Sr–Nd–Pb–O isotopic constraints for mantle source characteristics and petrogenesis. *Journal of Petrology* **40**, 1399–1424.

Murphy, MA, Yin, A, M., HT, Duerr, SB, Chen, Z, Ryerson, FJ, Kidd, WSF, Wang, X & Zhou, X (1997) Did the Indo-Asian collision alone create the Tibetan Plateau? *Geology* **25**, 719–722.

Owens, TJ & Zandt, G (1997) Implications of crustal property variations for models of Tibetan plateau evolution. *Nature* **387**, 37–43.

Patiño Douce, AE, Johnston, AD & Rice, JM (1993) Octahedral excess mixing properties in biotite; a working model with applications to geobarometry and geothermometry. *American Mineralogist* **78**, 113–131.

Patiño Douce, AE & McCarthy, TC (1998) Melting of crustal rocks during continental collision and subduction. In: Hacker, BR & Liou, JG (eds.) *When Continents Collide: Geodynamics and Geochemistry of Ultrahigh-Pressure Rocks*. pp. 27–55. Kluwer Academic Publishers: Dordrecht.

Powell, R & Holland, TJB (1988) An internally consistent dataset with uncertainties and correlations: 3. Applications to geobarometry, worked examples and a computer program. *J. Metamorphic Geol.* **6**, 173–204.

Ravna, EJK & Terry, MP (2004) Geothermobarometry of phengite-kyanite-quartz/coesite eclogites. *Journal of Metamorphic Geology*.

Schaltegger, U, Zeilinger, G, Frank, M & Burg, J-P (2002) Multiple mantle sources during island arc magmatism: U-Pb and Hf isotopic evidence from the Kohistan arc complex, Pakistan. *Terra Nova* **14**, 461–468.

Schwab, M, Ratschbacher, L, Siebel, W, McWilliams, M, Lutkov, V, Minaev, V, Chen, F, Stanek, K, Nelson, B, Frisch, W & Wooden, JL (2004) Assembly of the Pamirs: Age and origin of magmatic belts from the southern Tien Shan to the southern Pamirs and their relation to Tibet. *Tectonics* **23**, TC4002, doi:10.1029/2003TC001583.

Sclater, JG, Jaupart, C & Galson, D (1980) The heat flow through oceanic and continental crust and the heat loss of the Earth. *Reviews of Geophysics and Space Physics* **18**, 269-311.

Searle, M, Corfield, RI, Stephenson, B & McCarron, J (1997) Structure of the North Indian continental margin in the Ladakh-Zaskar Himalayas: Implications for the timing of obduction of the Spontang ophiolite, India-Asia collision and deformation events in the Himalaya. *Geological Magazine* **134**, 297-316.

Searle, M, Hacker, BR & Bilham, R (2001) The Hindu Kush seismic zone as a paradigm for the creation of ultrahigh-pressure diamond and coesite-bearing rocks. *Journal of Geology* **109**, 143–154.

Searle, MP (1991) *Geology and tectonics of the Karakoram Mountains*. John Wiley & Sons Ltd: West Sussex.

Spera, FJ (1984) Carbon dioxide in petrogenesis III: role of volatiles in the ascent of alkaline magmas with special reference to xenolith-bearing mafic lavas. *Contributions to Mineralogy and Petrology* **88**, 217–232.

Strecker, MR, Frisch, W, Hamburger, MW, Ratschbacher, L, Semiletkin, S, Sturchio, N & Zamoruyev, A (1995) Quaternary deformation in the Eastern Pamirs, Tadzhikistan and Kyrgyzstan. *Tectonics* **14**, 1061-1079.

Taylor, SR & S. M. McLennan, SM (1985) *The continental crust; its composition and evolution*. Blackwell Scientific Publications: Oxford.

Tropper, P, Essene, EJ, Sharp, ZD & Hunziker, JC (1999) Application of K-feldspar-jadeite-quartz barometry to eclogite facies metagranites and metapelites in the Sesia Lanzo Zone (Western Alps, Italy). *Journal of Metamorphic Geology* **17**, 195-209.

Turner, S, Arnaud, N, Liu, J, Rogers, N, Hawkesworth, C, Harris, N, Kelley, S, Van Calsteren, P & Deng, W (1996) Post-collision, shoshonitic volcanism on the Tibetan Plateau; implications for convective thinning of the lithosphere and the source of ocean island basalts. *Journal of Petrology* **37**, 45-71.

Vlasov, NG, Dyakov, YA & Cherev, ES (1991) Geological map of the Tajik SSR and adjacent territories, 1:500,000. Leningrad.

Walsh, EO & Hacker, BR (2004) The fate of subducted continental margins: Two-stage exhumation of the high-pressure to ultrahigh-pressure Western Gneiss complex, Norway. *Journal of Metamorphic Geology* **22**, 671-689.

Yund, RA (1997) Rates of grain boundary diffusion through enstatite and forsterite reaction rims. *Contributions to Mineralogy and Petrology* **126**, 224–236.

Zanchi, A & Gritti, D (1996) Multistage structural evolution of Northern Karakoram (Hunza region, Pakistan). *Tectonophysics* **260**, 145-165.

Table 1. Mineral assemblages and modes.

Sample	gar	cpx	ky	mus	bio	san	qtz	rut	hb	plg	carb	apat
<b>337A</b>	11±5	52±5			22±5	13±10		1				
<b>1154A</b>	37±2	59±3			(g)		2	1	(g)	(g)		<1
<b>1154B</b>	19±2	36±2	6±1			6±1	32±2	1	(g)	(g)		<1
<b>1283A</b>	26±5	62±2				2	5±1	1	(g)			4±2
<b>1283B</b>	24±5	36±5			(g)	35±10	1	1	2(g)	(g)	2	
<b>1309</b>	10±2	44±2	10±1			16±1	19±1	1	(g)	(g)		
<b>1503A</b>	16±16		4±4			19±14	60±35	1				
<b>1503B</b>	32±2		10±1	(g)	(g)	11±1	46±2	1				
<b>1503C</b>	24±5		15±5			9±2	51±10	2				
<b>2014</b>		17±8			80±7	3±1						<1

Determined by point counting on an optical microscope. “±” for major minerals indicate variation apparent at the scale of a thin section.

(g), found only as inclusion in garnet.

Table 2. Mineral Compositions

Sample	337A	337A	337A	337A	337A	337A	337A	337A
Mineral	gar	gar	cpx	cpx	kfs	bio	bio	kfs
	core	rim	core	rim	core	hi Ti	lo Ti	rim
Analysis	172	40	43	70	129	85	20pl	130
SiO <sub>2</sub>	37.59	37.71	50.73	51.82	64.33	35.51	35.55	62.12
TiO <sub>2</sub>	0.26	0.16	0.60	0.79	<	7.95	2.42	<
Al <sub>2</sub> O <sub>3</sub>	21.57	21.84	6.00	9.69	19.11	14.53	17.89	19.42
Cr <sub>2</sub> O <sub>3</sub>	0.05	0.05	0.12	0.05	<	0.05	<	0.05
Fe <sub>2</sub> O <sub>3</sub>	2.93	2.56	5.69	4.17	0.09	0.00	0.00	0.21
FeO	23.20	23.46	5.70	4.90	<	16.60	16.51	<
MnO	0.72	0.67	0.12	0.07	<	0.04	0.17	<
MgO	7.25	7.69	9.95	8.06	<	11.27	13.47	<
CaO	6.50	5.72	17.80	13.50	0.26	<	0.09	0.24
Na <sub>2</sub> O	<	<	3.18	5.61	4.81	0.48	1.08	0.97
K <sub>2</sub> O	<	<	<	<	9.78	9.26	8.67	15.14
Totals	100.1	99.9	99.9	98.3	98.4	95.7	95.9	98.2
Oxygens	12	12	6	6	8	11	11	8
Si	2.91	2.92	1.89	1.91	2.96	2.68	2.66	2.93
Ti	0.02	0.01	0.02	0.02	<	0.45	0.14	<
Al	1.97	1.99	0.26	0.42	1.04	1.29	1.58	1.08
Cr	0.00	0.00	0.00	0.00	<	0.00	0.00	0.00
Fe <sub>3</sub>	0.17	0.15	0.16	0.12	0.00	<	0.00	<
Fe <sub>2</sub>	1.50	1.52	0.18	0.15	0.00	1.05	1.03	<
Mn	0.05	0.04	0.00	0.00	<	0.00	0.01	<
Mg	0.84	0.89	0.55	0.44	<	1.27	1.50	<
Ca	0.54	0.47	0.71	0.53	<	0.00	0.01	0.01
Na	<	<	0.23	0.40	0.43	<	0.16	0.09
K	<	<	<	<	0.58	0.89	0.83	0.91
Sum	8.0	8.0	4.0	4.0	5.0	7.6	7.9	5.0

Table 2. Mineral Compositions (continued)

Sample	1154A	1154A	1154A	1154A	1154A	1154A
Mineral	gar	gar	cpx	bio	amph	plag
	core	rim				
Analysis	80	180	52	181	157	178
SiO <sub>2</sub>	39.55	39.10	54.19	36.20	40.46	61.40
TiO <sub>2</sub>	0.13	0.11	0.42	3.40	1.77	0.00
Al <sub>2</sub> O <sub>3</sub>	22.01	22.50	13.68	15.03	13.93	24.06
Cr <sub>2</sub> O <sub>3</sub>	<	<	0.04	0.08	0.08	<
Fe <sub>2</sub> O <sub>3</sub>	1.1	1.47	<	0.62	3.63	0.56
FeO	17.78	17.38	4.4	17.50	10.58	0.00
MnO	0.4	0.46	<	0.20	0.15	<
MgO	9.48	9.25	7.54	12.96	11.82	<
CaO	9.62	9.77	13.44	0.08	10.49	4.59
Na <sub>2</sub> O	<	<	6.02	0.65	3.07	7.86
K <sub>2</sub> O	<	<	<	8.70	1.46	2.40
Totals	100.1	100.1	99.8	95.4	97.5	100.9
Oxygens	12	12	6	11	23	8
Si	2.96	2.95	1.93	2.74	6.04	2.73
Ti	0.01	0.01	0.01	0.19	0.20	0.00
Al	1.97	2.00	0.57	1.34	2.45	1.26
Cr	<	<	0.00	0.01	0.01	<
Fe <sub>3</sub>	0.10	0.08	<	0.04	0.41	0.02



Fe2	1.11	1.10	0.13	1.11	1.32	0.00
Mn	0.03	0.03	<	0.01	0.02	<
Mg	1.20	1.04	0.40	1.46	2.63	<
Ca	0.63	0.79	0.51	0.01	1.68	0.22
Na	<	<	0.42	0.10	0.89	0.68
K	<	<	<	0.84	0.28	0.14
Sum	8.0	8.0	4.0	7.8	15.9	5.0

Table 2. Mineral Compositions (continued)

Sample	1154B	1154B	1154B	1154B
Mineral	gar	gar	cpx	kfs
	core	rim		
Analysis	555	601	93	343pl
SiO2	39.03	39.02	53.63	62.87
TiO2	0.21	0.12	0.57	0.03
Al2O3	22.17	22.40	14.70	19.73
Cr2O3	0.05	<	<	<
Fe2O3	1.59	1.47	0.00	0.04
FeO	19.33	18.15	4.66	0.00
MnO	0.46	0.39	0.04	<
MgO	9.01	8.30	6.81	<
CaO	8.57	10.41	12.92	0.08
Na2O	<	<	6.38	1.94
K2O	<	<	<	13.70
Totals	100.4	100.3	99.7	98.4

Oxygens	12	12	6	8
Si	2.95	2.95	1.91	2.93
Ti	0.01	0.01	0.02	1.09
Al	1.98	2.00	0.62	0.00
Cr	0.00	<	<	<
Fe3	0.09	0.08	0.00	0.00
Fe2	1.22	1.15	0.14	0.00
Mn	0.03	0.03	0.00	<
Mg	1.02	0.94	0.36	<
Ca	0.70	0.84	0.49	0.00
Na	<	<	0.44	0.18
K	<	<	<	0.82
Sum	8.0	8.0	4.0	5.0

Table 2. Mineral Compositions (continued)

Sample	1283B 1283B	1283B	1283B	1283B	1283B	1283B	1283B	1283B	1283B	1283B	1283B
Mineral	gar glass? core	gar rim	cpx	bio	mu	plg	kfs	san	amph	carbo- nate	
Analysis	48	58	76	139	225	62	95	157	224	189	77
SiO2	39.21	39.19	54.19	35.82	50.08	53.04	65.15	64.79	35.02	<	0.13
TiO2	0.21	0.13	0.50	0.40	0.27	0.01	<	0.02	0.09	<	<
Al2O3	21.52	21.98	13.86	17.12	24.18	29.20	18.96	17.77	17.89	<	<
Cr2O3	<	0.06	<	<	0.00	<	<	0	<	<	<
Fe2O3	0.95	0.86	0.00	2.62	2.26	0.44	<	0.18	7.24	<	<
FeO	20.06	20.58	5.95	13.35	4.29	<	<	0	10.19	13.79	0.64
MnO	0.51	0.48	0.03	0.16	0.02	<	<	0	0.24	0.33	0.06
MgO	7.46	8.17	6.74	15.01	2.81	<	<	0.01	8.72	11.88	0.33
CaO	10.23	8.81	12.10	0.03	0.46	11.51	0.10	0.01	11.33	32.44	51.43

Na2O	<	<	6.48	0.29	0.16	4.69	2.12	0.02	2.06	<	0.73
K2O	<	<	<	9.55	9.71	0.29	13.92	17.21	2.18	<	<
Totals	100.2	100.3	99.9	94.4	94.3	99.2	100.3	100.0	95.0	58.56	53.36
Oxygens	12	12	6	11	11	8	8	8	23	1	1
Si	2.99	2.98	1.94	2.71	3.43	2.42	2.98	3.01	5.47	<	0.00
Ti	0.01	0.01	0.01	0.02	0.01	0.00	<	0.00	0.01	<	<
Al	1.94	1.97	0.58	1.53	1.95	1.57	1.02	0.97	3.29	<	<
Cr	<	0.00	<	<	0.00	<	<	0.00	<	<	<
Fe3	0.06	0.05	0.00	0.15	0.12	0.02	<	0.01	0.85	<	n.d.
Fe2	1.28	1.31	0.18	0.84	0.25	<	<	0.00	1.33	0.18	0.01
Mn	0.03	0.03	0.00	0.01	0.00	<	<	0.00	0.03	0.00	0.00
Mg	0.85	0.93	0.36	1.69	0.29	<	<	0.00	2.03	0.28	0.01
Ca	0.84	0.72	0.46	0.00	0.03	0.56	0.01	0.00	1.90	0.54	0.95
Na	<	<	0.45	0.04	0.02	0.42	0.19	0.00	0.62	<	0.02
K	<	<	<	0.92	0.85	0.02	0.81	1.02	0.44	<	<
Sum	8.0	8.0	4.0	7.9	7.0	5.0	5.0	5.0	16.0	1.0	1.0

Table 2. Mineral Compositions (continued)

Sample	1309	1309	1309	1309	1309	1309	1309
Mineral	gar core	gar rim	cpx	amph	plag	kfs	carbo- nate
Analysis	168	132	158	239	97	172	106
SiO2	38.99	39.02	54.47	45.38	51.90	64.18	<
TiO2	0.14	0.17	0.5	0.16	<	<	<
Al2O3	21.86	21.86	15.66	4.40	30.54	18.88	<
Cr2O3	0.03	<	<	0.08	<	<	<
Fe2O3	1.07	0.79	<	0.00	0.83	<	<
FeO	21.6	21.66	5.52	29.14	0.00	<	<
MnO	0.63	0.62	0.04	0.55	0.00	0.00	<
MgO	6.65	6.60	5.6	14.31	0.02	0.00	<
CaO	9.82	9.89	11.02	1.90	12.89	0.11	61.02
Na2O	0.01	<	7.41	0.04	3.90	1.77	<
K2O	0.01	<	<	0.44	0.70	14.07	0.20
Totals	100.8	100.6	100.2	96.4	100.8	99.1	61.2
Oxygens	12	12	6	23	8	8	3
Si	2.98	2.98	1.93	7.08	2.35	2.97	<
Ti	0.01	0.01	0.013	0.02	<	<	<
Al	1.97	1.97	0.654	0.81	1.63	1.03	<
Cr	<	<	<	0.01	<	<	<
Fe3	0.06	0.05	<	0.00	0.03	<	<
Fe2	1.38	1.39	0.164	3.80	0.00	<	<
Mn	0.04	0.04	0.001	0.07	0.00	0.00	<
Mg	0.76	0.75	0.296	3.33	0.00	0.00	<
Ca	0.8	0.81	0.418	0.32	0.63	0.01	1.00
Na	<	<	0.509	0.01	0.34	0.16	<
K	<	<	<	0.09	0.04	0.83	<
Sum	8.0	8.0	4.0	15.5	5.0	5.0	1.0

Table 2. Mineral Compositions (continued)

Sample	1503A	1503A	1503A
Mineral	gar core	gar rim	kfs kfs
Analysis	109	119	129
SiO2	38.75	38.51	65.43

TiO2	0.04	0.04	0.01
Al2O3	22.14	21.91	19.71
Cr2O3	0.05	0.10	<
Fe2O3	0.80	1.09	<
FeO	25.97	25.59	<
MnO	0.49	0.50	<
MgO	10.32	10.00	<
CaO	1.13	1.69	0.47
Na2O	<	<	4.32
K2O	<	<	10.01
Totals	99.7	99.4	100.0

Oxygens	12	12	8
Si	2.97	2.97	2.96
Ti	0.00	0.00	0.00
Al	2.00	1.99	1.05
Cr	0.00	0.01	<
Fe3	0.05	0.06	<
Fe2	1.67	1.65	<
Mn	0.03	0.03	<
Mg	1.18	1.15	<
Ca	0.09	0.14	0.02
Na	<	<	0.38
K	<	<	0.58
Sum	8.0	8.0	5.0

Table 2. Mineral Compositions (continued)

Sample	1503B	1503B	1503B	1503B	1503B
Mineral	gar	bio	mus	mus	kfs
			hi-Si	lo-Si	
Analysis	284	282	396	291	292
SiO2	38.85	36.40	53.59	47.10	64.70
TiO2	0.04	6.40	0.01	0.00	0.00
Al2O3	22.06	16.49	21.55	37.11	19.91
Cr2O3	0.04	0.06	<	<	<
Fe2O3	0.00	0.00	0.02	0.65	<
FeO	26.25	14.20	2.86	0.25	<
MnO	0.51	0.00	0.02	0.00	<
MgO	10.03	12.95	5.17	1.05	<
CaO	1.26	<	0.19	<	0.25
Na2O	<	0.45	<	0.17	3.87
K2O	<	9.30	10.07	10.40	10.90
Totals	99.1	96.3	96.80	96.8	99.7

Oxygens	12	11	11	11	8
Si	3.00	2.68	3.64	3.06	2.95
Ti	0.00	0.36	0.00	0.00	0.00
Al	2.01	1.43	1.72	2.84	1.07
Cr	0.00	0.00	<	<	<
Fe3	0.00	0.00	0.00	0.03	<
Fe2	1.69	0.88	0.16	0.01	<
Mn	0.03	0.00	0.00	0.00	<
Mg	1.15	1.42	0.52	0.10	<
Ca	0.10	<	0.01	<	0.01
Na	<	0.06	<	0.02	0.34
K	<	0.88	0.87	0.86	0.63

Sum	8.0	7.7	6.9	6.9	5.0
-----	-----	-----	-----	-----	-----

Table 2. Mineral Compositions (continued)

Sample	2014	2014	2014
Mineral	bio	kfs	cpx
Analysis	175	146	1v1
SiO2	38.01	65.17	53.30
TiO2	4.51	0.07	0.33
Al2O3	13.03	17.66	1.22
Cr2O3	0.04	0.00	0.08
Fe2O3	0.00	0.12	0.54
FeO	11.74	<	7.34
MnO	0.13	<	0.14
MgO	17.18	<	13.71
CaO	0.03	<	22.79
Na2O	0.36	0.06	0.63
K2O	9.56	16.82	<
Totals	94.6	99.93	100.07

Oxygens	11	8	6
Si	2.83	3.02	1.98
Ti	0.25	0.00	0.01
Al	1.14	0.97	0.05
Cr	0.00	0.00	0.00
Fe3	0.00	<	0.02
Fe2	0.73	<	0.23
Mn	0.01	<	0.00
Mg	1.90	<	0.76
Ca	0.00	<	0.91
Na	0.05	0.01	0.05
K	0.91	1.00	<

Sum	7.8	5.0	4.0
-----	-----	-----	-----

Table 3. Bulk compositions.

	337A	1154A	1154B	1283A	1283B	1309	1503A	1503B	1503C
Calculated from mineral compositions and modal abundances (Normalized to 100%, carbonates excluded.)									
SiO <sub>2</sub>	49.4	49.4	64.6	51.0	53.9	60.6	79.9	69.3	70.8
Al <sub>2</sub> O <sub>3</sub>	12.8	16.5	14.5	15.1	17.5	18.7	9.9	15.7	16.5
TiO <sub>2</sub>	3.3	1.3	1.2	1.4	1.2	1.2	1.0	1.0	2.0
FeO*	11.2	9.6	5.6	9.3	7.7	4.7	4.3	8.5	6.5
Cr <sub>2</sub> O <sub>3</sub>	0.0	0.1	0.0	0.0	0.0	0.0	0.0	0.0	0.0
MnO	0.1	0.2	0.1	0.2	0.2	0.1	0.1	0.2	0.1
MgO	8.0	8.0	4.0	6.3	4.5	3.1	1.6	3.2	2.3
CaO	8.3	11.4	6.7	12.2	6.8	5.8	0.3	0.5	0.4
Na <sub>2</sub> O	3.2	3.6	2.4	4.3	3.2	3.6	0.7	0.4	0.3
K <sub>2</sub> O	3.6	0.1	0.8	0.3	5.0	2.3	2.2	1.3	1.0
forced sum	100	100	100	100	100	100	100	100	100

Sample	337A	1154B	1283B	1309†	1503C	2014
<b>ICP-ES</b>						
SiO <sub>2</sub>	46.29	57.71	50.99	56.05	71.48	44.63
TiO <sub>2</sub>	2.95	1.10	1.16	0.90	0.93	3.72
Al <sub>2</sub> O <sub>3</sub>	12.26	18.76	18.21	19.12	15.10	13.09
Fe <sub>2</sub> O <sub>3</sub>	12.22	7.88	10.88	7.15	6.38	12.17
MnO	0.111	0.131	0.209	0.120	0.106	0.107
MgO	8.24	4.65	4.74	3.72	2.01	13.97
CaO	9.12	7.22	8.19	6.70	0.66	4.61
Na <sub>2</sub> O	2.69	2.29	2.16	2.46	0.36	0.47
K <sub>2</sub> O	4.15	1.77	4.15	3.80	2.47	8.03
P <sub>2</sub> O <sub>5</sub>	0.52	0.21	0.42	0.20	0.03	0.14
Sum	98.56	101.72	101.11	100.21	99.52	100.94
LOI	1.71	2.77	1.86	2.90	1.29	3.29
Sr	734	539	676	738	139	707
Ba	1077	478	857	829	366	5825
Ni	138	47	21	32	113	178
Cr	337	95	33	56	108	189
Zr	238	242	289	284	352	59
Y	21	20	31	19	33	5
<b>ICP-MS</b>						
Li	27.8	25.5	28.7	57.1	8.80	67.5
Be	2.34	1.23	1.40	5.63	1.57	4.73
Sc	21.2	20.6	29.6	18.1	14.0	12.5
V	208	175	201	125	77	232
Cr	349	90.4	36.7	57.9	58.5	196
Co	42.0	25.5	29.9	22.6	23.9	45.7
Ni	148	39.7	16.1	28.9	131	200
Cu	34.7	31.5	50.9	38.1	20.7	11.9
Zn	136	18.7	26.8	58.7	18.4	138
Rb	129	39.1	190	101	78.5	548
Sr	712	516	673	719	139	675
Y	19.9	18.6	29.4	17.5	32.6	3.0
Cs	1.37	0.457	2.32	17.4	0.782	8.69
Ba	1068	471	854	815	372	5746
Pb	13.6	2.26	4.63	21.45	31.6	6.76
Th	1.71	0.353	3.57	2.80	5.08	2.00
U	0.482	0.251	0.785	0.407	1.30	0.421
La	43.9	13.1	19.2	23.7	19.4	18.1
Ce	93.5	30.0	43.4	46.9	36.9	37.0
Pr	11.6	3.86	5.42	5.51	3.97	4.44
Nd	45.5	16.5	21.9	21.3	14.8	17.5

Sm	9.10	3.85	5.18	4.34	4.16	3.37
Eu	2.89	1.16	1.51	1.51	1.19	1.10
Gd	7.78	4.03	5.81	4.11	4.97	2.39
Tb	1.08	0.617	0.93	0.630	0.86	0.313
Dy	4.85	3.56	5.44	3.36	5.47	1.26
Ho	0.815	0.702	1.09	0.649	1.18	0.196
Er	1.94	1.90	2.92	1.72	3.45	0.473
Yb	1.29	1.66	2.58	1.49	3.51	0.333
Lu	0.187	0.255	0.398	0.227	0.562	0.048

Oxides in wt%, elements in ppm. LOI = loss on ignition.

Boston University analysts: Terry Plank, Louise Bolge, Serin Duplantis, Florencia Meana-Prado.

† this sample contains 5-10% host lava

Table 4. Calculated pressures and temperatures.

<b>Rock</b>	<b>T (°C)</b>	<b>T method</b>	<b>P (kbar)</b>	<b>P method</b>
<b>337A</b>	720–750	K00	20–25	assumed
	865–880	GCT96	20–25	assumed
	900–925	garnet–biotite	20–25	assumed
<b>1154A</b>	1010	K00	22.5	CaTs, using BM04
<b>1154A</b>	1050	GCT96	28.5	CaTs, using THERMOCALC
<b>1154A</b>	>1000	GCT96	>21.0	ab=jd+qz, $a_{ab}=1$
<b>1154B</b>	1040	K00	24.7	GCKQ
	1060	K00	28.0	ab=jd+qz, $a_{ab}$ from kfs, using HDR91
	1015	GCKQ	26.8	ab=jd+qz, $a_{ab}$ from kfs, using HDR91
<b>1283B</b>	1100	K00	28.5	ab=jd+qz, $a_{ab}$ from kfs, using HDR91
<b>1283B</b>	1130	GCT96	29.2	ab=jd+qz, $a_{ab}$ from kfs, using HDR91
<b>1309</b>	1065	K00	26.5	GCKQ
	1090	K00	30.4	ab=jd+qz, $a_{ab}$ from kfs, using HDR91
	1035	GCKQ, GCT96	28.8	ab=jd+qz, $a_{ab}$ from kfs, using HDR91
<b>1503</b>	1025–1060	PD98	2.1–3.0	PD98

BM04, Brandelik & Massonne (2004); GCT96, Ganguly *et al.* (1996); HDR91, Hovis *et al.* (1991); K00, Krogh Ravna (2000); GCKQ, garnet + quartz = clinopyroxene + kyanite (Ravna & Terry 2004); PD98, experimental results of Patiño Douce & McCarthy (1998). “>” are minima.

Table 5. Calculated physical properties.

Sample	0.01 GPa, 25°C <sup>1</sup>				2.8 GPa, 1075°C <sup>1</sup>			
	density (g/cm <sup>3</sup> )	V <sub>P</sub> (km/s)	V <sub>S</sub> (km/s)	ν	density (g/cm <sup>3</sup> )	V <sub>P</sub> (km/s)	V <sub>S</sub> (km/s)	ν
<b>337A</b>	3.25±0.08	7.20±0.14	4.04±0.09	0.27±0.00	3.25	7.08	3.85	0.29
<b>1154A</b>	3.57±0.01	8.32±0.01	4.75±0.01	0.26±0.00	3.54	8.14	4.52	0.28
<b>1154B</b>	3.21±0.02	7.44±0.04	4.46±0.02	0.21±0.00	3.19	7.64	4.31	0.26
<b>1283A</b>	3.47±0.02	8.13±0.03	4.67±0.01	0.25±0.00	3.44	7.99	4.45	0.27
<b>1283B</b>	3.20±0.07	7.45±0.15	4.17±0.10	0.27±0.00	3.20	7.38	4.01	0.28
<b>1309</b>	3.19±0.01	7.49±0.02	4.37±0.01	0.24±0.00	3.18	7.55	4.20	0.27
<b>1503A</b>	2.90±0.74	6.6±2.2	4.12±0.35	0.18±0.10	2.90	7.13	4.05	0.26
<b>1503B</b>	3.18±0.02	7.07±0.04	4.31±0.2	0.20±0.00	3.17	7.46	4.21	0.27
<b>1503C</b>	3.13±0.07	7.02±0.14	4.31±0.04	0.20±0.01	3.12	7.44	4.21	0.26
<b>2014</b>	3.00±0.03	6.23±0.12	3.40±0.08	0.29±0.00	3.02	6.16	3.24	0.31
<b>harz.</b> <sup>2</sup>	3.34	8.29	4.82	0.24	3.32	8.08	4.54	0.27
<b>lherz.</b> <sup>2</sup>	3.37	8.17	4.73	0.25	3.38	8.14	4.54	0.27

Calculated using formalism of Hacker & Abers (2004). Uncertainties are ±1 σ derived from thin-section scale variations in mineral mode (Table 1) only.

ν is Poisson's ratio.

1: Calculations at STP use alpha quartz, those at elevated P and T use beta quartz.

2: Garnet harzburgite and garnet lherzolite from Hacker *et al.* (2003).



Figure 1

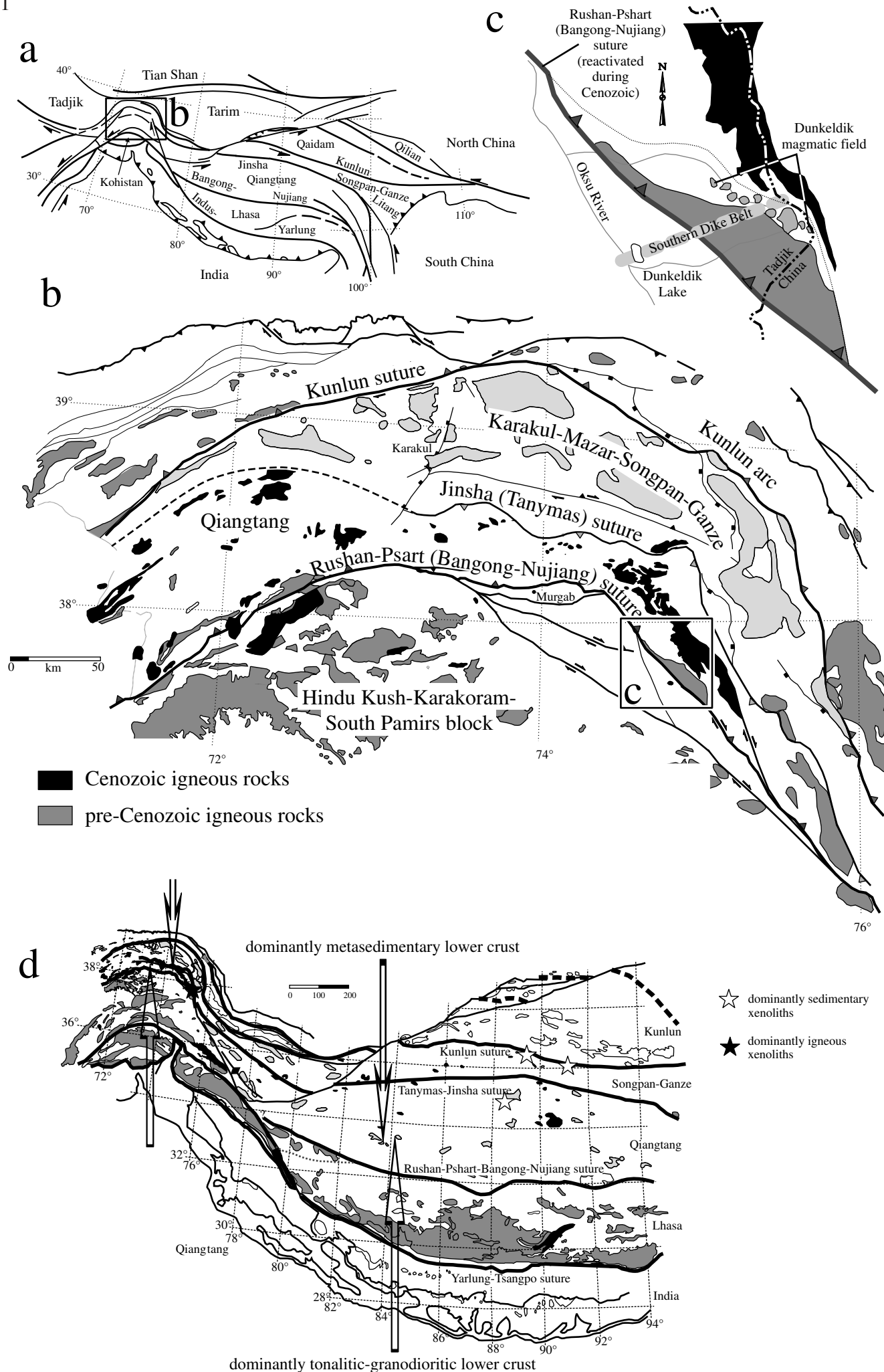
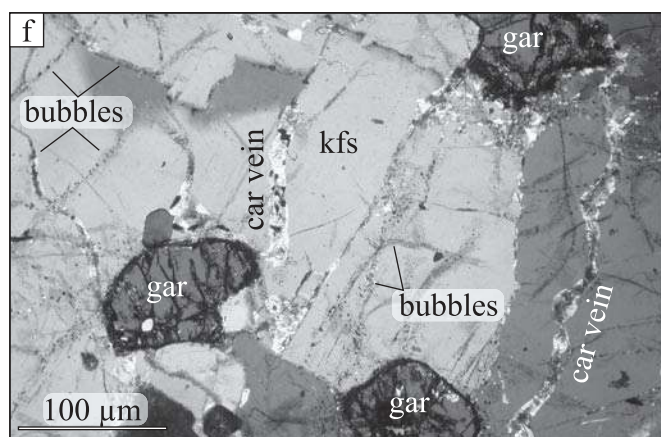
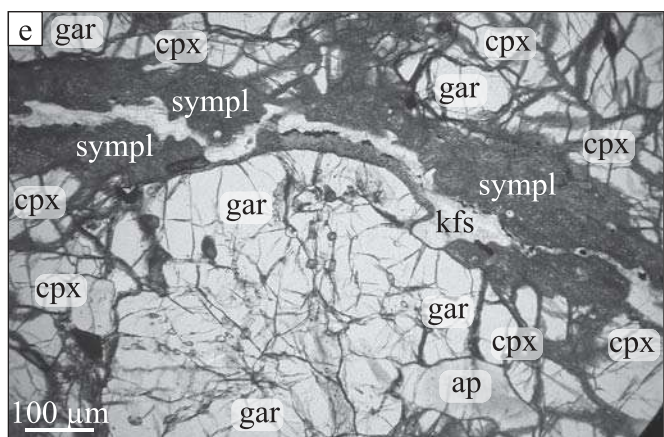
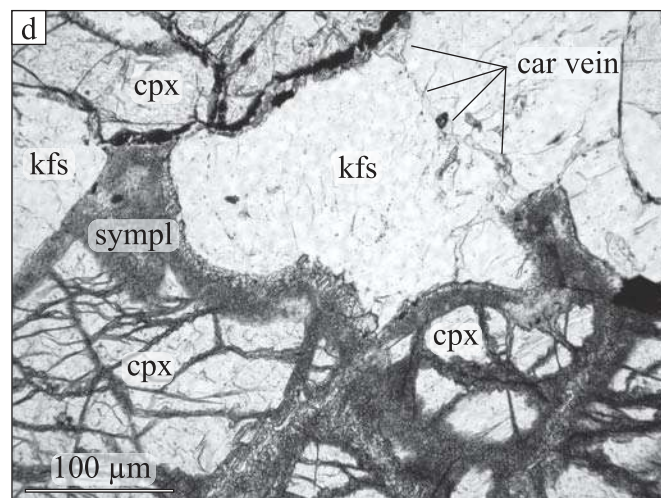
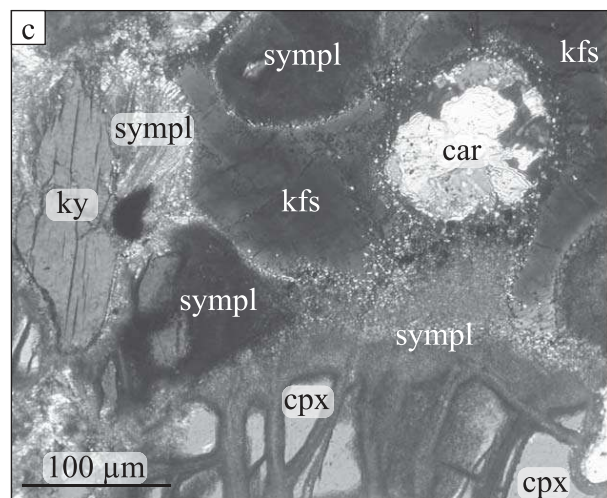
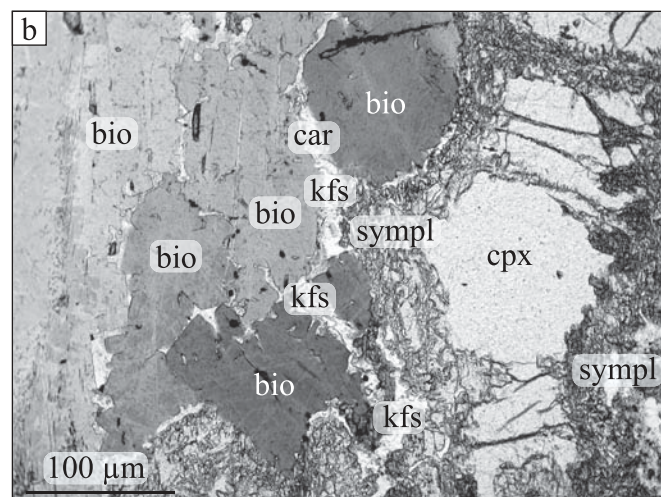
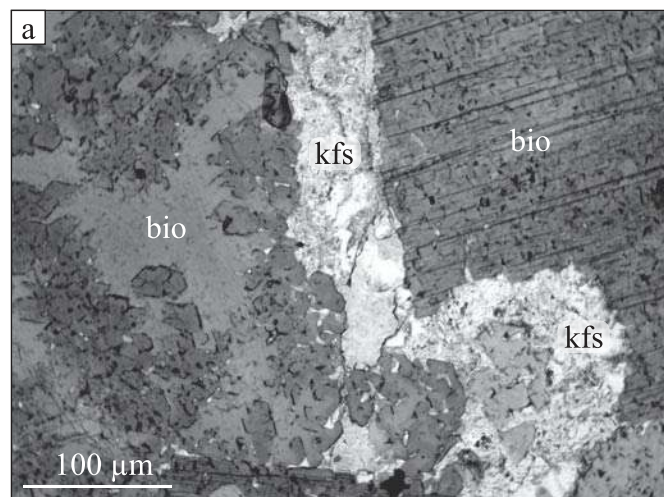
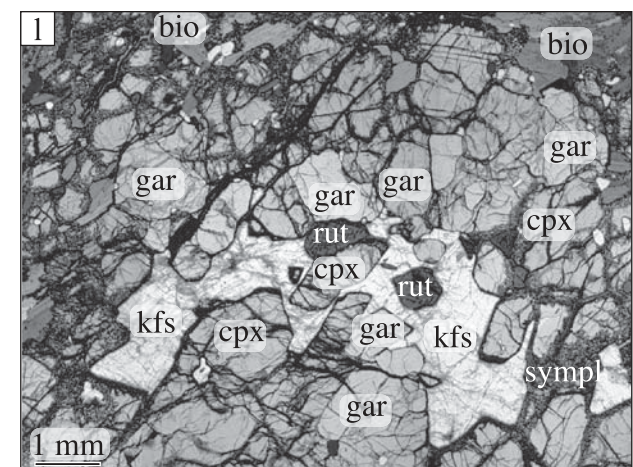
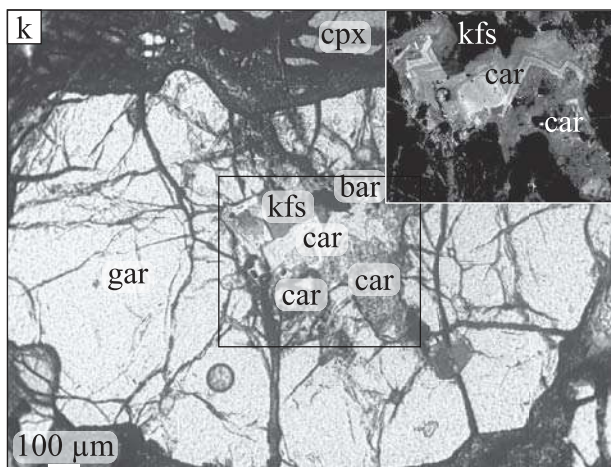
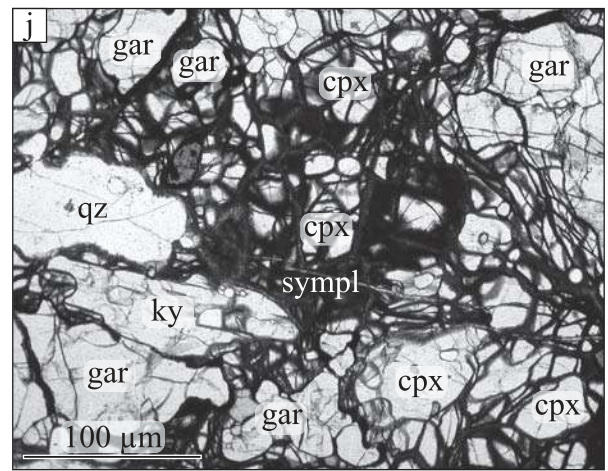
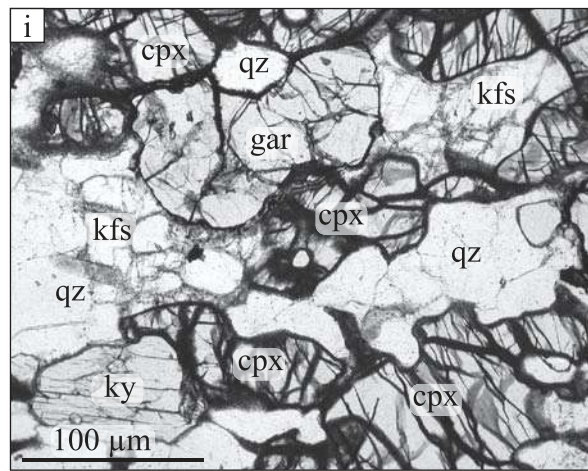


Figure 2







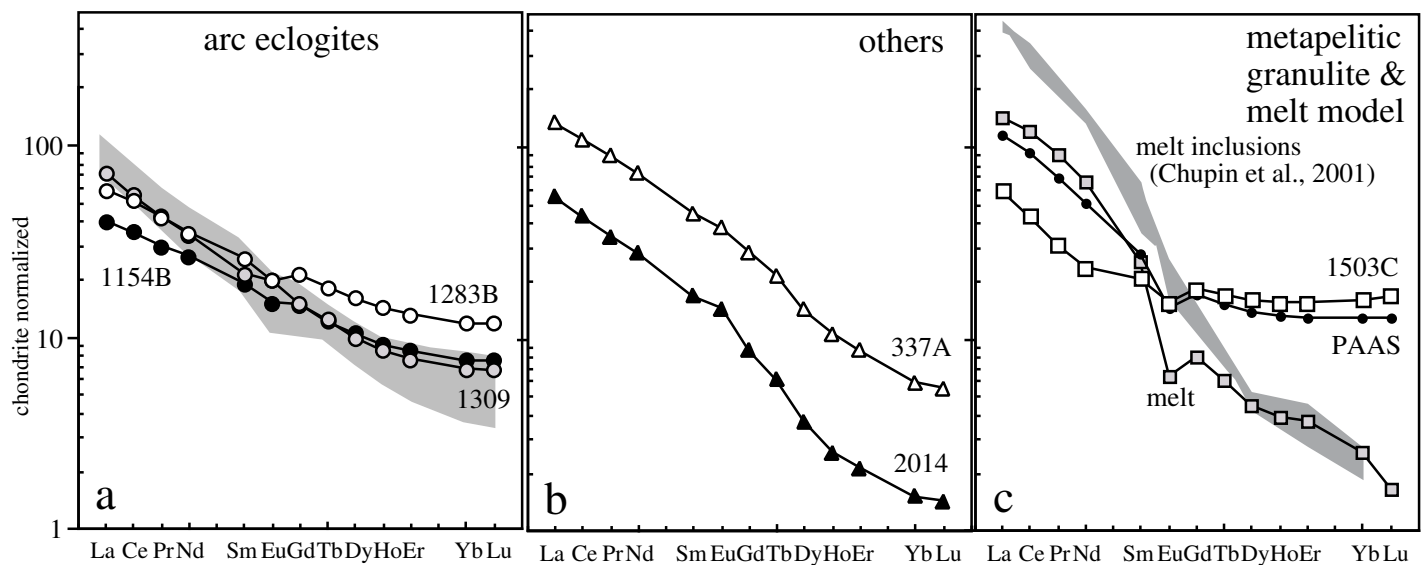
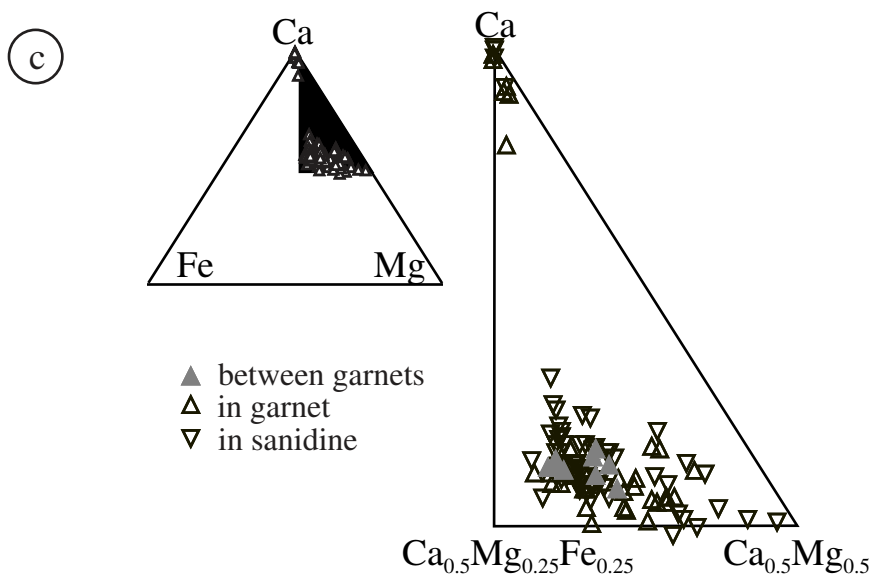
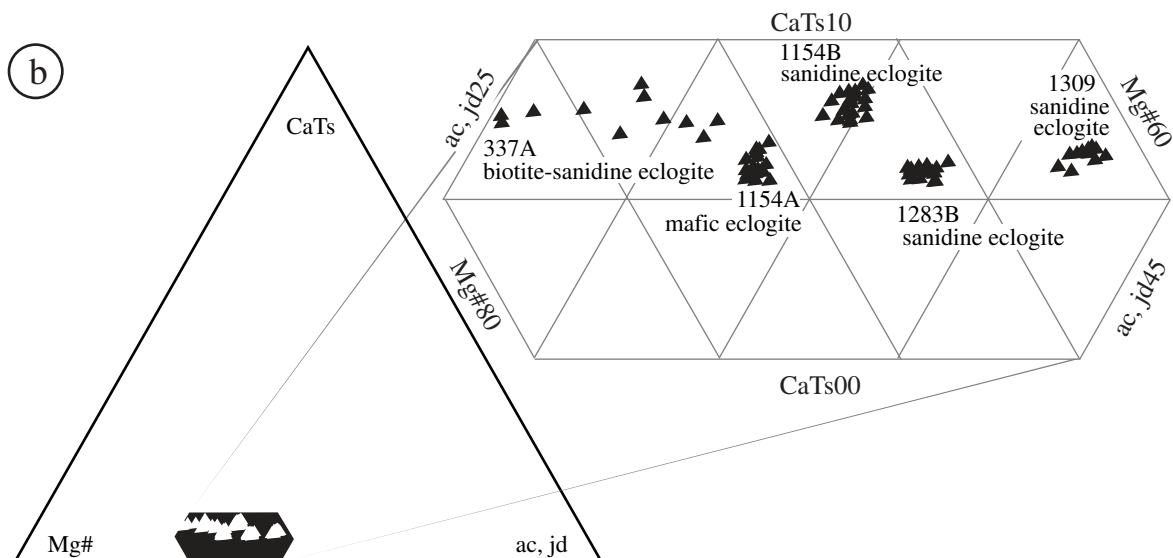
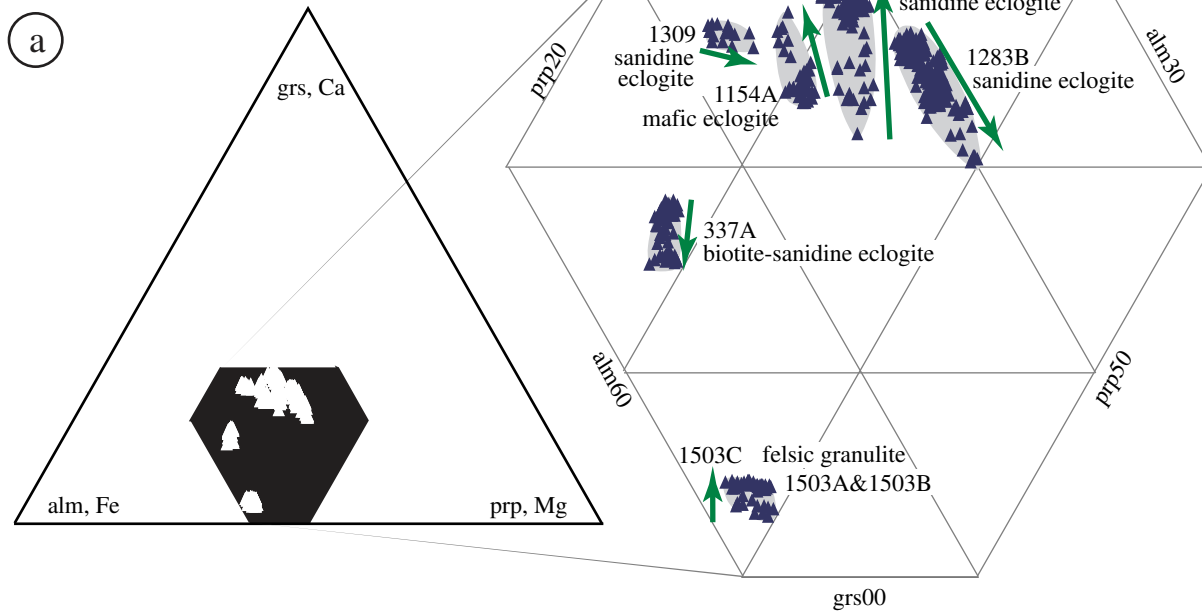


Figure 3. Rare earth element patterns for Pamir xenoliths (data in Table 3). a) Samples with arc affinity. Sanidine eclogites 1283B and 1154B have nearly parallel REE patterns. 1309 has a steeper REE pattern due to host lava contamination. Shaded field indicates patterns from Andean andesites (Kay et al., 1991) and Sierran granodiorites (Frost, 1987), which could be similar to eclogite protoliths. b) 337A sanidine eclogite; 2014 glimmerite. c) 1503C metapelitic granulite; PAAS (post-Archean average shale from Taylor & McLennan, 1985). If 1503C had an initial pattern like PAAS, it has lost 40% melt of composition shown. Calculation first dilutes PAAS with quartz such that it contains 71.5 wt% SiO<sub>2</sub> like 1503C, then calculates melt from mass balance. Melt fractions > 42% are required to create a smooth melt pattern. Shaded field indicates patterns of glass inclusions found in quartz crystals from similar granulite xenoliths from the Pamir (Chupin et al., 2001).



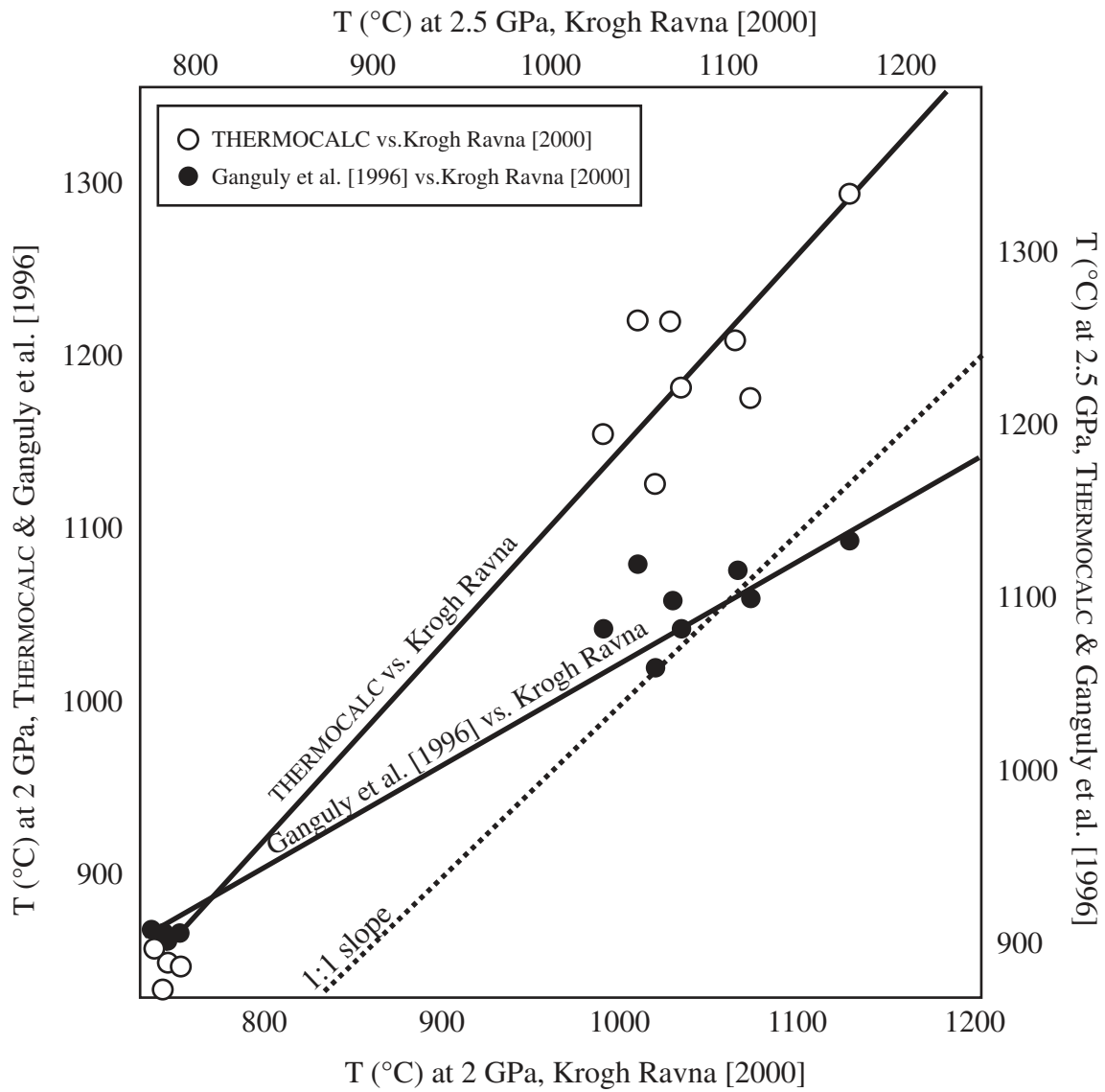


Figure 5. Temperatures calculated for all samples from three garnet-clinopyroxene calibrations at 2.0 GPa (left and bottom axes) and 2.5 GPa (right and top axes). We use the more conservative (cooler) temperatures from Ganguly et al. [1996].

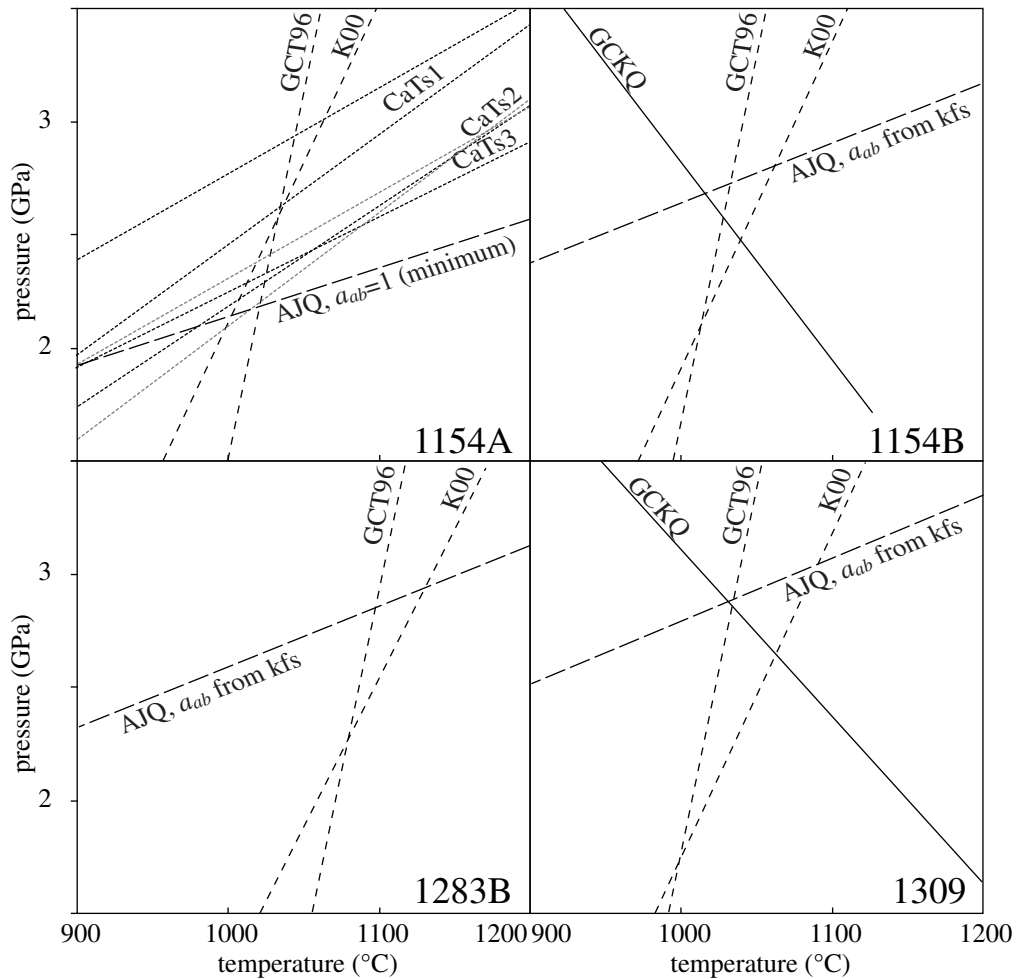


Figure 6. Calculated pressures and temperatures for individual samples. AJQ, albite = jadeite + quartz reaction, from THERMOCALC. CaTs, Ca-tschermak component in clinopyroxene in equilibrium with garnet (there are 2 reactions for each calibration; the Mg-endmember reactions have gentler slopes than the Fe-endmember reactions); 1 = THERMOCALC, 2 = PTGIBBS with solution model of Ganguly and Saxena [1984], 3 = PTGIBBS with solution model of Berman [1990], 3 . GCKQ, garnet-clinopyroxene-kyanite-quartz, after Ravna and Terry [2004]. GCT96, garnet-clinopyroxene Fe-Mg exchange, after Ganguly et al. [1996]. K00, garnet-clinopyroxene Fe-Mg exchange, after Krogh Ravna [2000].



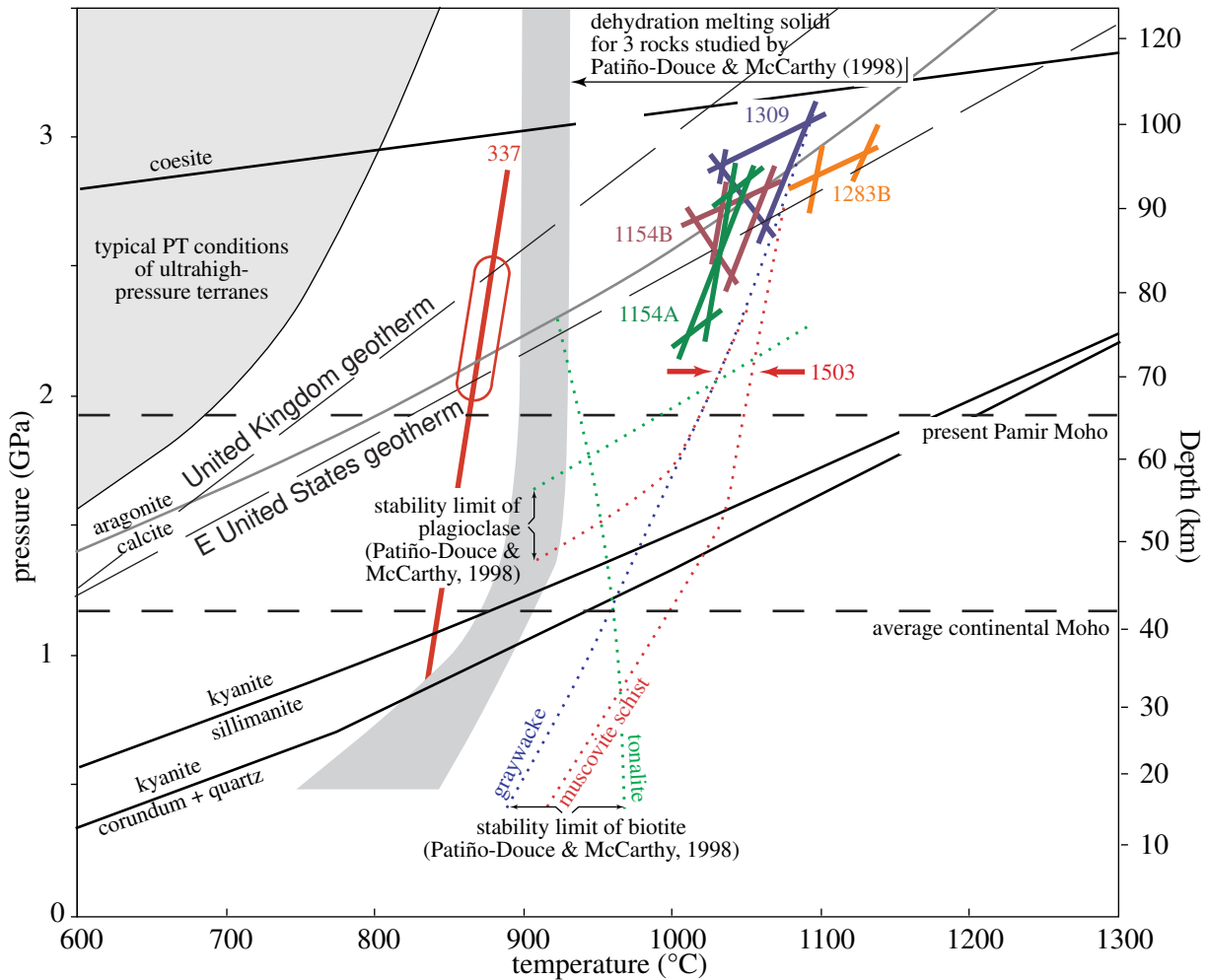


Figure 7. Calculated pressures and temperatures. Solid, colored lines show garnet-clinopyroxene thermometers (K00 and GCT96; positive slope), garnet + quartz = clinopyroxene + kyanite thermometer (negative slope) and feldspar-breakdown barometers. Pressure converted to depth using global density profile of Christensen and Mooney [1995]. Endmember reactions involving coesite, aragonite, and kyanite were calculated using THERMOCALC. Dotted lines are experimentally determined mineral stability limits. Arrows indicate temperature range for 1503 at 2.1 GPa. Geotherms for UK and western US from Sclater et al. [1980].



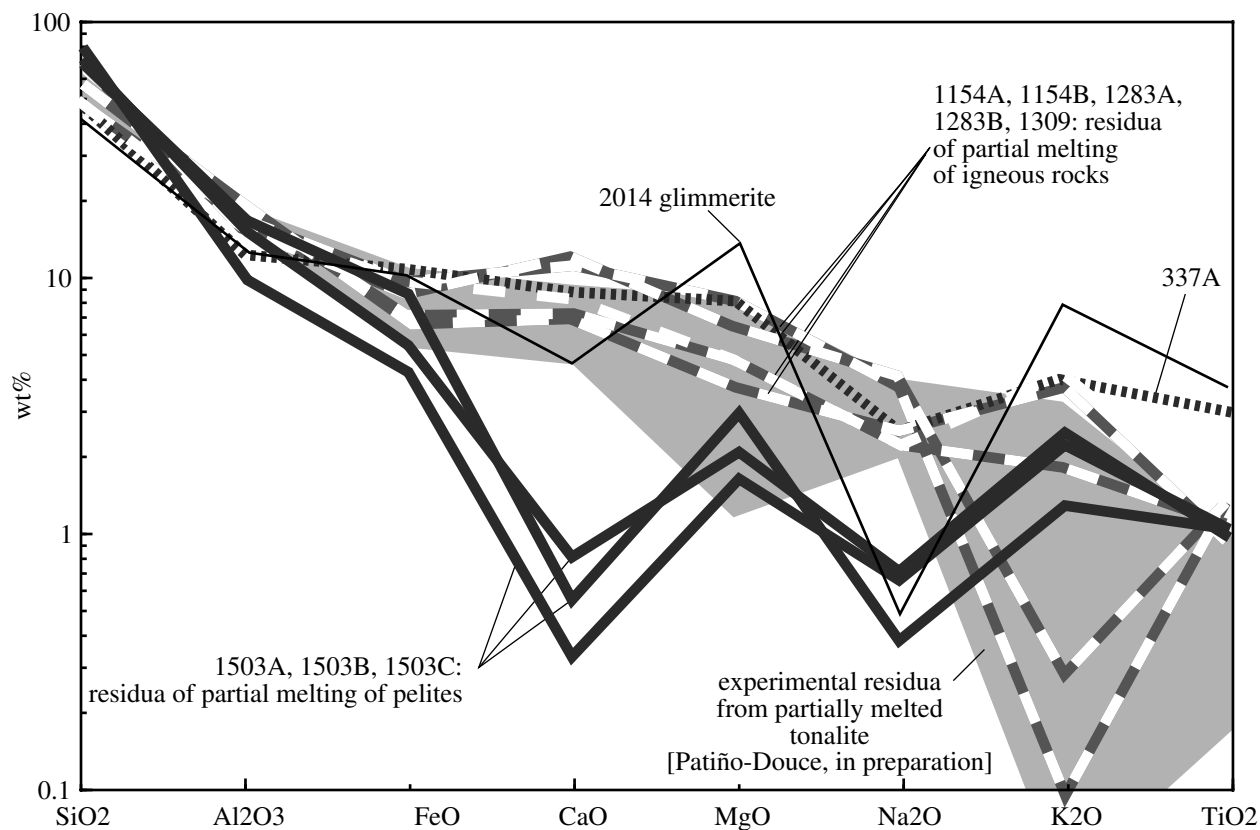


Figure 8. Bulk compositions of some of the Pamir xenoliths are similar to residua produced in partial melting experiments of calc-alkaline tonalite at 21-32 kbar and 950-1150°C [grey field; Patiño-Douce, in preparation].

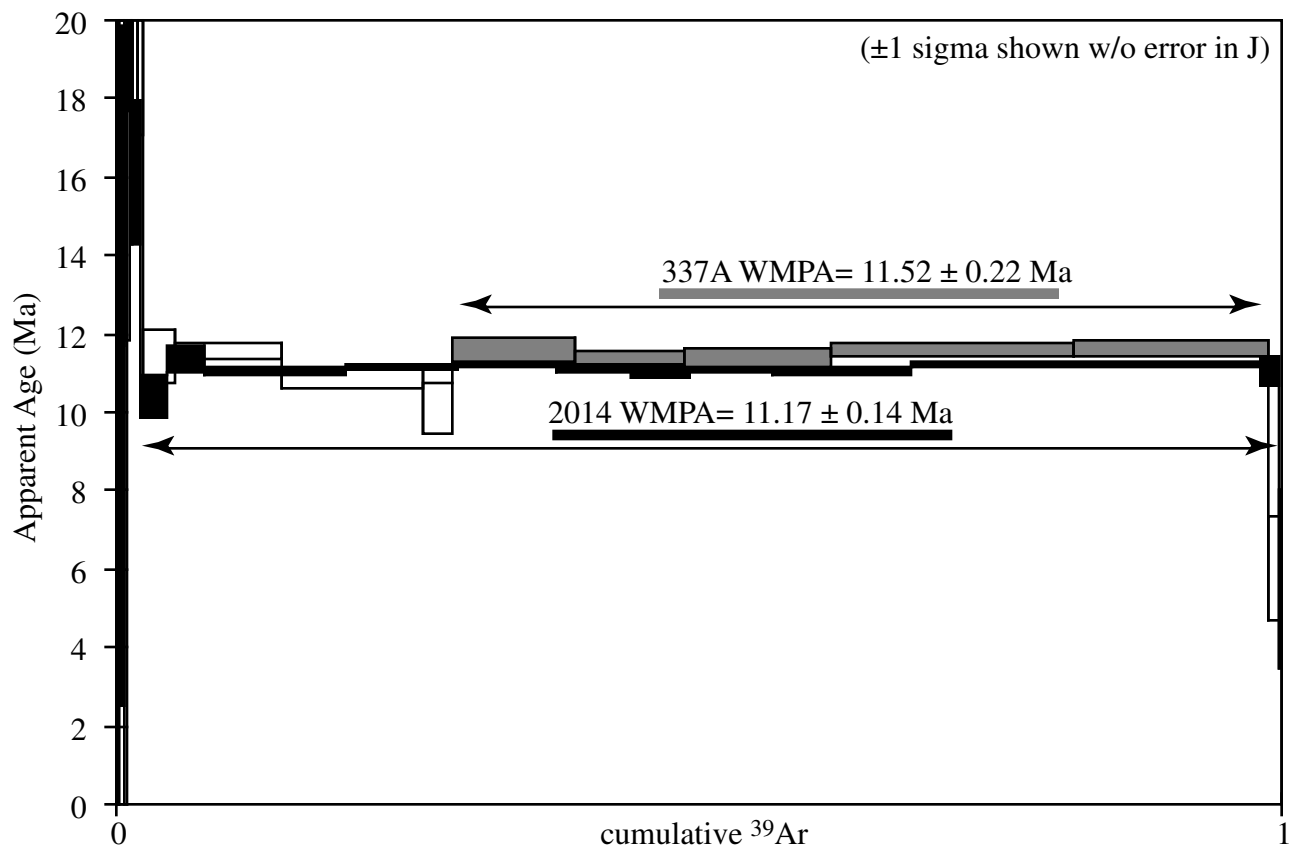


Figure 9.  $^{40}\text{Ar}/^{39}\text{Ar}$  apparent age spectra of biotites shows eruption ages of 11.2 and 11.5 Ma.

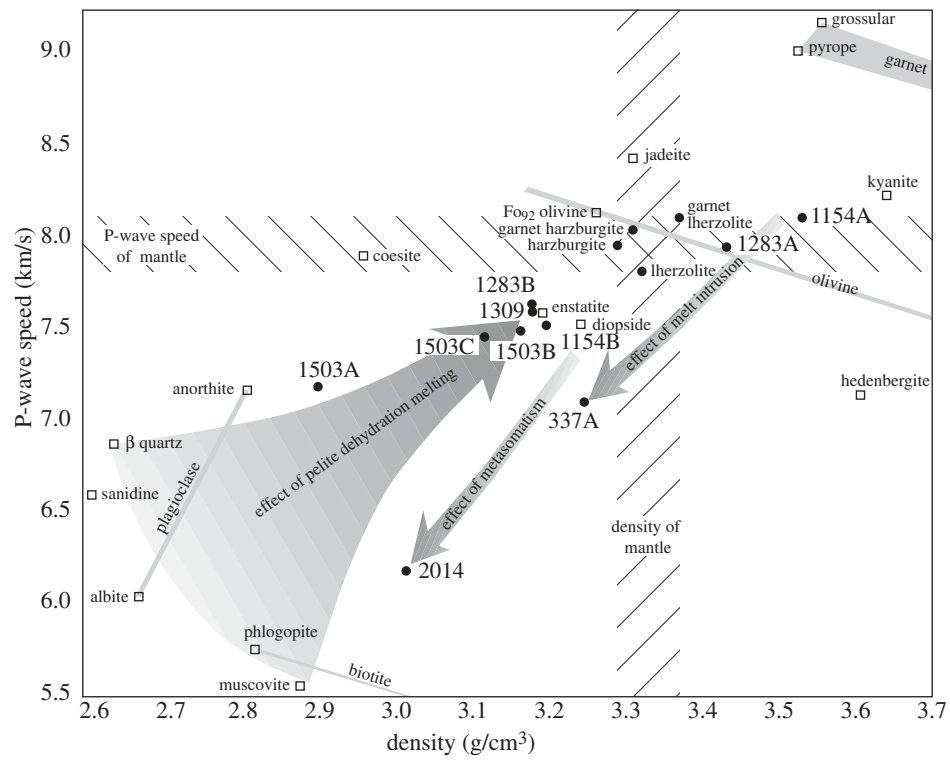
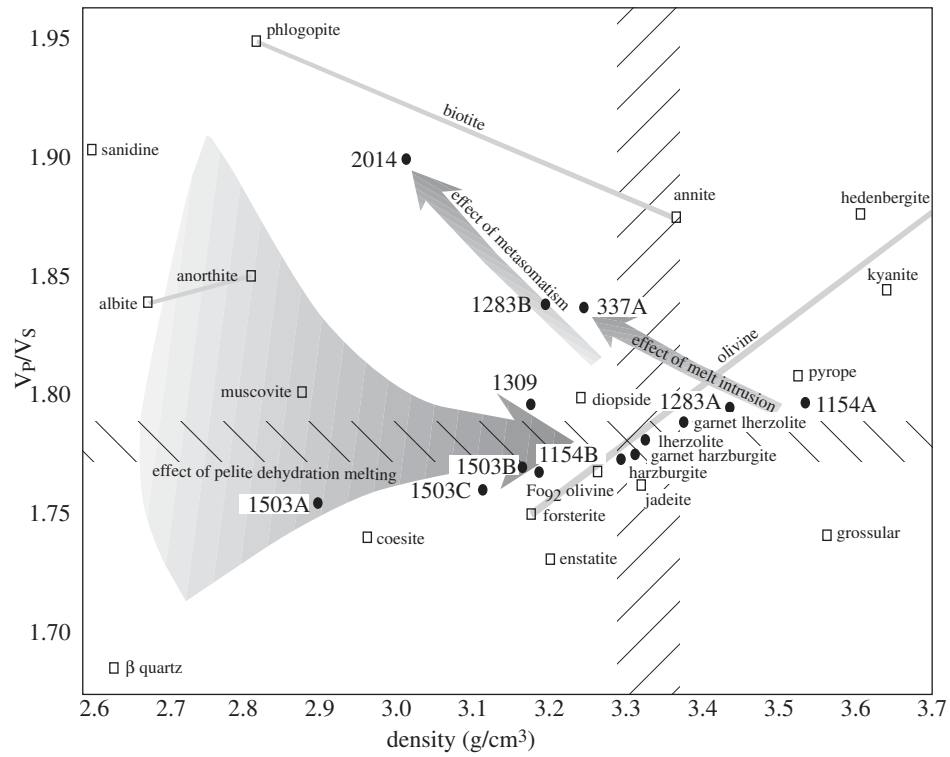


Figure 10. Calculated densities, P-wave speeds, and  $V_p/V_s$  ratios for 2.8 GPa and 1050°C.

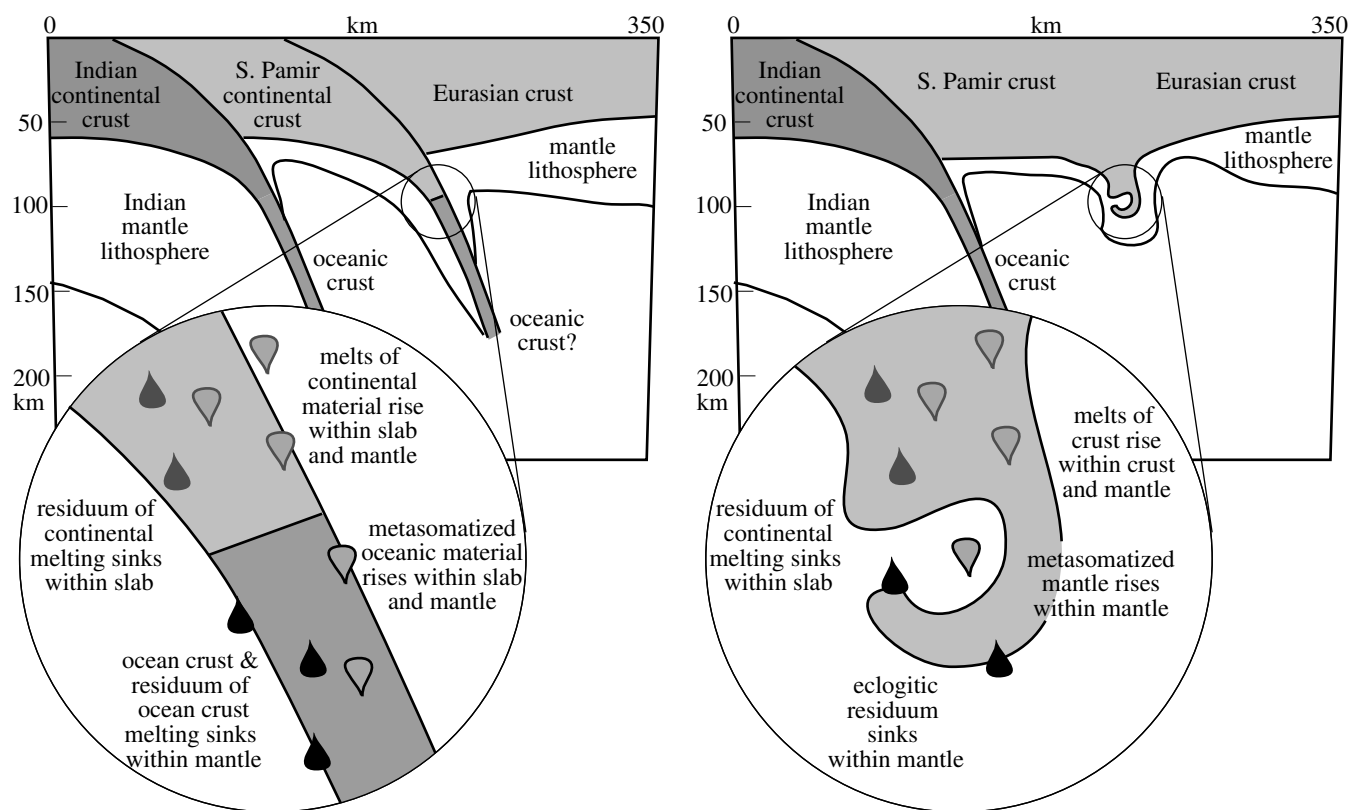


Figure 11. Melting and metasomatism beneath the Pamir in the Eocene(?)–Miocene.